Journal of Structural Geology 150 (2021) 104404

Contents lists available at ScienceDirect

Journal of Structural Geology

journal homepage: www.elsevier.com/locate/jsg

The evolution of slate microfabrics during progressive accretion of foreland basin sediments

Ismay Vénice Akker [a,*], Alfons Berger [a], Christoph E. Schrank [b], Michael W.M. Jones [c], Cameron M. Kewish [d,e], Jop Klaver [f], Marco Herwegh [a]

[a] Institute of Geological Sciences, University of Bern, Baltzerstrasse 1+3, 3012, Bern, Switzerland
[b] School of Earth and Atmospheric Sciences, Queensland University of Technology, Queensland, 4000, Australia
[c] Central Analytical Research Facility, Queensland University of Technology, Queensland, 4000, Australia
[d] Australian Nuclear Science and Technology Organisation, Australian Synchrotron, Victoria, 3168, Australia
[e] Department of Chemistry and Physics, La Trobe Institute for Molecular Science, La Trobe University, Victoria, 3086, Australia
[f] Energy & Mineral Resource Group, RWTH Aachen University, Lochnerstrasse 4-20, 52064, Aachen, Germany

ARTICLE INFO

Keywords:
Microstructure
Phyllosilicates
Accretionary wedge
Foliation

ABSTRACT

Here, we study slate microfabrics from the exhumed accretionary wedge of the central European Alps and focus on the development of foliation. High-resolution micrographs from novel BIB-SEM imaging and Synchrotron X-ray Fluorescence Microscopy are analysed with 2D auto-correlation functions to quantify the geometry and spacing of slate microfabrics along a metamorphic gradient covering the outer and inner wedge (200–330 °C). The sedimentary layering primarily controls the morphology of the slate microfabrics. However, from outer to inner wedge, a fabric evolution is observed where diagenetic foliations gradually transform to secondary continuous and spaced foliations. With increasing metamorphic grade, the amount of recrystallized phyllosilicate grains and their interconnectivity increase, as does clast/microlithon elongation (aspect ratios up to 11), while foliation spacing decreases to <20 μm. This foliation evolution under non-coaxial deformation involves a combination of mechanical rotation of phyllosilicates, fracturing, and fluid-assisted pressure-dissolution-precipitation creep. The latter is the dominant deformation mechanism at T > 230 °C and accommodates background strain in the inner wedge. The evolving microstructural anisotropy is interpreted to lead to strain weakening by structural softening and may provide preferential fluid pathways parallel to the foliation, enabling the dehydration of large rock volumes in accretionary sediment wedges undergoing prograde metamorphism.

1. Introduction

Studies from active and exhumed accretionary wedges show that the deformational style, intensity, and structures in the wedge are a function of lithification and burial (e.g., Dielforder et al., 2016a; Ditullio and Byrne, 1990; Kimura et al., 2007). During progressive accretion, the fabric and composition of the sediments change due to soft-sediment compaction followed by diagenetic to low-grade metamorphic reactions accompanied by deformation, such as the smectite to illite transition, pressure solution, and cementation (e.g., Dielforder et al., 2016a; Hyndman et al., 1993; Moore and Saffer, 2001; Saffer and Tobin, 2011). As a result, sediments turn into sedimentary and then metasedimentary rocks with well-developed secondary foliations. Consequently, their mechanical and transport properties change dramatically (Donath, 1961, 1964; McLamore and Gray, 1967). These changes in material properties define the deformational style and structures in the wedge and have important implications for fluid flow and seismic behaviour (Moore and Saffer, 2001; Moore and Vrolijk, 1992; Oleskevich et al., 1999; Saffer and Tobin, 2011; Ujiie and Kimura, 2014).

With respect to the progressive deformation in the accretionary wedge, one well-studied mechanical consequence in such sediments is the formation of foliations made of aligned phyllosilicates (Ditullio and Byrne, 1990; Norris and Bishop, 1990; Palazzin et al., 2016; Raimbourg et al., 2009). The morphology and spacing of foliation, which change as function of metamorphic temperature and strain (Norris and Bishop, 1990; van der Pluijm et al., 1998), make a useful tool for textural mapping (Turnbull et al., 2001). Starting in the 1970s, four possible end-member processes enabling the development of foliation on the

* Corresponding author.
E-mail address: ismay.akker@geo.unibe.ch (I.V. Akker).

https://doi.org/10.1016/j.jsg.2021.104404
Received 9 November 2020; Received in revised form 6 June 2021; Accepted 20 June 2021
Available online 24 June 2021

grain-scale were laid out: passive rotations, recrystallization, pressure solution, and anisotropic growth. Passive rotations of anisotropic grains in a viscous matrix (e.g., Etheridge and Hobbs, 1974; Gray, 1978; Groshong Jr, 1988; Herwegh and Jenni, 2001; White and Knipe, 1978) and recrystallization (e.g., Bons, 1988; Cosgrove, 1976; Durney, 1972a; Durney, 1972b; Marlow and Etheridge, 1977) were identified as important processes responsible for the development of foliation. Passive rotations are important at low temperatures and strains, while dissolution and neocrystallization become increasingly important at elevated temperatures (van der Pluijm et al., 1998). Pressure solution is an important mass transport mechanism during foliation formation (Cosgrove, 1976; Durney, 1972a, 1972b; Plessman, 1964). Bons et al. (1990) showed that phyllosilicate grain boundaries act as fluid pathways for such fluid-assisted mass transport during foliation formation, with estimates of volume loss during foliation development of up to 50% (Bons (1988) and references therein; Etheridge et al. (1983); Kawabata et al. (2007); Rahl et al. (2011)). Finally, anisotropic growth of newly formed phyllosilicates may facilitate foliation development (Knipe, 1981).

Laboratory experiments have shown that the interconnectivity of weak phases such as phyllosilicates forming foliations reduces the strength of rocks (Niemeijer and Spiers, 2005; Shea Jr and Kronenberg, 1993; Shea and Kronenberg, 1992), and has even been proposed as a mechanism for enabling plate tectonics (Montési, 2013). At the brittle-ductile transition, the microphysical deformation mechanisms of the phyllosilicates include a combination of frictional sliding along the foliation facilitated by pressure solution processes of stronger minerals. The respective bulk deformation mechanism is called frictional-viscous flow (Bos et al., 2000; Bos and Spiers, 2001; Handy, 1990; Niemeijer and Spiers, 2005). However, rigid clasts and microlithons embedded in the phyllosilicate matrix may deform by microfracturing, which promotes grain size reduction as well as pressure solution (Den Hartog and Spiers, 2014). Pervasive microfracturing is commonly observed in natural rocks from accretionary wedges (Elphick et al., 2021; Fagereng et al., 2011; Meneghini et al., 2009; Palazzin et al., 2016).

Here, we quantitatively document the microfabric changes during foliation development in phyllosilicate-rich sediments of an accretionary wedge as a function of increasing metamorphism. Such data are required to unravel how different deformation processes contribute to foliation development as a function of metamorphic grade and progressive accretion. To this end, we study a sample series from naturally deformed slates from the Northern Alpine Foreland Basin (Eastern Switzerland, European Alps). The samples have been collected along a metamorphic gradient covering the outer and inner wedge of the exhumed Alpine paleo-accretionary prism. Applying the autocorrelation function (ACF) to high-resolution images from Broad Ion Beam Scanning Electron Microscopy (BIB-SEM) and Synchrotron X-ray Fluorescence Microscopy (SXFM), we measured foliation spacing, mineral orientations, and ACF aspect ratios. These data quantify the relative intensity of secondary fabrics and can, under certain circumstances, serve as a proxy for finite strain. SXFM yields micro-chemical maps that permit the linking of deformation processes in foliation forming minerals with the expected chemical mass transport processes.

2. Geological background

Late stages of subduction and subsequent continental collision between the European and Adriatic plate resulted in the formation of the Northern Alpine Foreland Basin, in which the (syn)orogenic Infrahelvetic Flysch Units (IFU) were deposited. The sedimentation ages of these units range from the upper Cretaceous to the Eocene (Lihou and Allen, 1996). The IFU were subsequently frontally accreted into the orogenic wedge (Dielforder et., 2016a). From north to south, an increasing metamorphic grade is recorded from the Northhelvetic Flysch (NHF) to the Southhelvetic Flysch, and finally to the Ultrahelvetic Flysch from, respectively, 200 °C/∼ 0.2 GPa to 330 °C/∼ 0.3 GPa. The peak metamorphic temperatures are established from data from calcite-dolomite thermometry (Ebert et al., 2007), Raman spectroscopy on carbonaceous material (Lahfid et al., 2010), and fluid inclusion data (Rahn et al., 1995). They suggest very-low grade metamorphism for the three different Flysch units (Frey et al., 1974, 1980). Greenschist facies was the highest peak metamorphic grade reached, but it is only found in the southernmost Ultrahelvetic units (Hunziker et al., 1986), which are not investigated in this study.

Deformation during the early stages of frontal accretion was dominated by soft-sediment deformation through particulate flow (Dielforder et., 2016a). Later stages of deformation in the IFU, from the mid-Oligocene to Miocene, are characterised by several researchers. Milnes and Pfiffner (1977) divided: (a) The Pizol phase; in this stage, the exotic strip sheets Sardona and Blattengrat were thrust onto the NHF by compressional tectonics. According to these authors, any penetrative structures formed during this deformation phase are not visible due to overprinting by later deformation phases. (b) The Cavistrau phase, in which the allochthonous Subhelvetic unit was emplaced. Deformation in this phase is only local (mountain Cavistrau) and therefore not of importance to this study. (c) The Calanda phase; in this Upper Oligocene stage, the IFU was folded, and a penetrative axial plane cleavage developed simultaneously with thrusting. Gasser and Den Brok (2008) have proposed that two foliations (F1 and F2) divide the Calanda phase: F1, in which the formation of an S1 axial plane cleavage belonging to the major folds was formed, and F2, in which an S2 foliation parallel to the overturned limb of the F1 folds formed, cutting S1 consistently. The deformation in the Calanda phase occurred under peak metamorphic greenschist conditions (Frey et al., 1974), with high strain localized in narrow zones. This is particularly evident from the Glarus thrust, which emplaced the Glarus nappe on top of the IFU along an extremely localized out-of-sequence crustal-scale shear zone (see Ebert et al. (2007) and references therein). This emplacement indicates the end of the imbrication of the IFU (Herwegh et al., 2008). The IFU were further deformed ductilely and overthrust by the Helvetic Nappes during (d) the Ruchi phase, a late-stage retrograde reactivation of the Glarus thrust. At that time, a crenulation cleavage formed. The deformation during this stage is strongly related to lithology and pre-existing structures formed during the Calanda phase (Milnes and Pfiffner, 1977). In this final stage, after the emplacement of the Helvetic Nappes, all the geological structures were deformed on the retrograde metamorphic path by doming of the crystalline Aar Massif (Berger et al., 2020; Nibourel et al., 2018; Pfiffner et al., 2011; Schmid, 1975).

3. Methodology

This work capitalises on a large collection of samples amassed during the PhD studies of Dielforder et al. (2016b) and Akker (2020) on the IFU in the Glarus Alps, eastern Switzerland. Here, we present analyses of slate samples representative of the most phyllosilicate-rich layers, deliberately excluding quartz- and carbonate-dominated intervals. Estimates of peak metamorphic temperature of our samples were obtained through along-strike extrapolation of the neighbouring temperature data from Ebert et al. (2007); Lahfid et al. (2010) and Rahn et al. (1995). The samples cover a metamorphic gradient from 200 to 330° (see an overview of sample locations and peak metamorphic temperatures in Fig. 1 and Table 1). For all samples, we first quantified the main mineralogy with X-ray powder diffraction (XRD). In a second step, we studied the microstructure of individually selected micro-layers with known composition from initial XRD analysis with the use of different microscopic techniques. Third, we used different image analysis tools to examine two main key elements making up the microstructure: foliation planes and clasts.

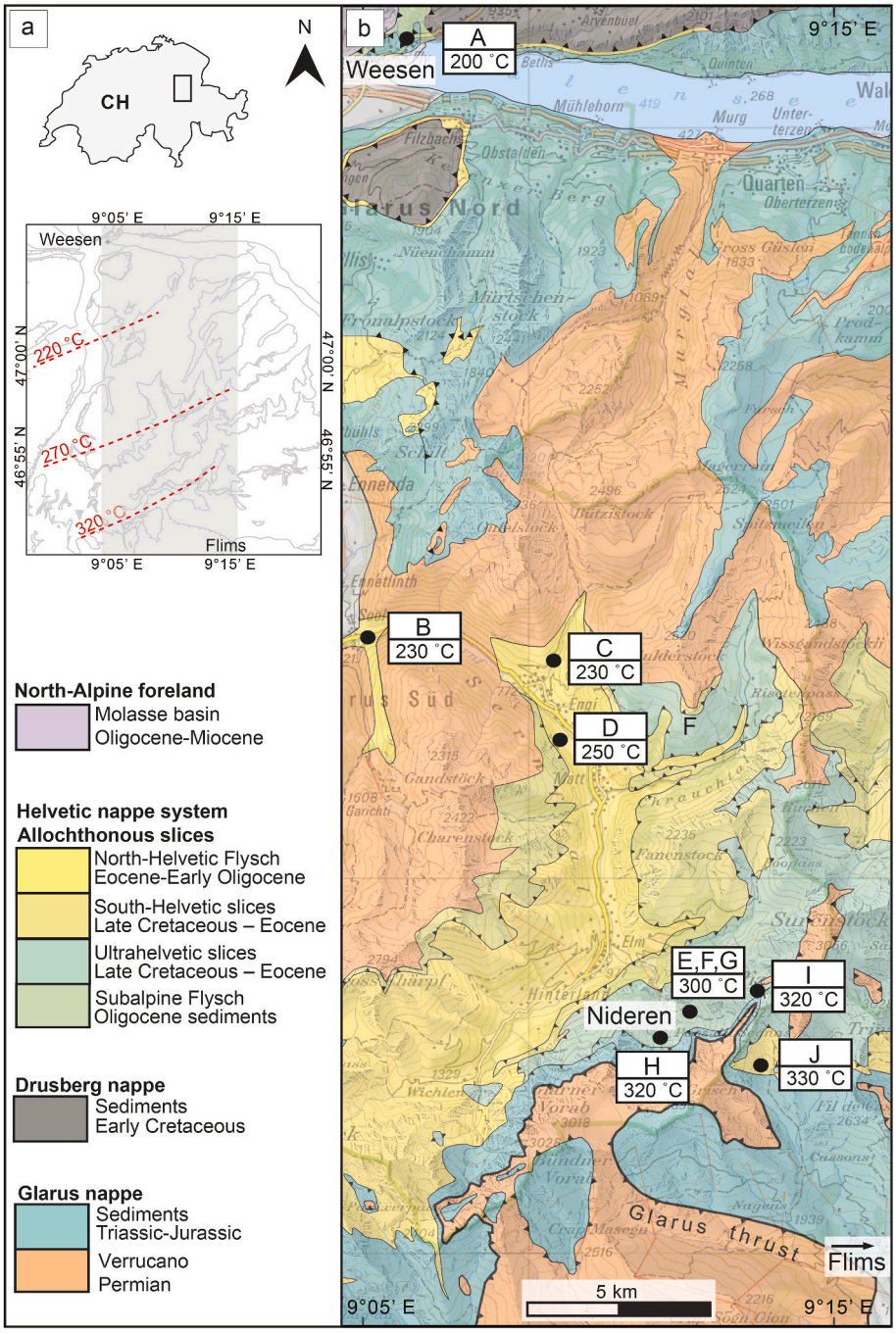

Fig. 1. Geological map of the study area and overview of peak metamorphic temperatures. a) Overview map with inferred isograds from the datasets from Ebert et al. (2007); Lahfid et al. (2010) and Rahn et al. (1995). Grey area represents the geological map as shown in (b). b) Geological map after Dielforder et al. (2016a) and references therein, with plotted sample locations and specific peak metamorphic temperature per sample. Peak metamorphic temperatures inferred after Ebert et al. (2007); Lahfid et al. (2010) and Rahn et al. (1995).

Table 1
Overview of investigated samples, with coordinates and peak metamorphic temperatures inferred from datasets of Ebert et al. (2007); Lahfid et al. (2010) and Rahn et al. (1995).

Sample ID	Sample label	Latitude	Longitude	Peak metamorphic temperature (°C)	Lithology
16W01	A	47°08′26.3″N	9°06′26.1″E	200	Calcite-rich slate
16SCH01B	B	46°59′47.2″N	9°05′20.9″E	230	Phyllosilicate-rich slate
16EN1A	C	46°59′13.9″N	9°09′17.6″E	230	Phyllosilicate-rich slate
17LP06	D	46°58′12.0″N	9°09′19.7″E	250	Phyllosilicate-rich slate
16N01A	E	46°54′11.0″N	9°11′21.3″E	300	Phyllosilicate-rich slate
17N3	F	46°54′23.6″N	9°12′01.4″E	300	Phyllosilicate-rich slate associated with vein-array
17N2	G	46°54′22.4″N	9°12′04.1″E	300	Phyllosilicate-rich slate
16MM01	H	46°53′29.0″N	9°11′22.4″E	320	Calcite-rich slate
16SP01	I	46°54′07.4″N	9°13′28.6″E	320	Quartz-rich slate
16SS01	J	46°53′02.8″N	9°13′28.8″E	330	Calcite-rich slate

3.1. Mineralogy

3.1.1. X-ray powder diffraction (XRD)

Although we sampled the phyllosilicate-richest lithologies, microstructural investigations showed considerable sample heterogeneity in terms of composition and structure within the slate layers (Fig. 2a). Such heterogeneities include sedimentary layering on the (sub)mm-scale, (micro)-veins and (micro)fractures. For XRD analysis (Table 2), samples with macroscopic calcite veins (>1 cm) were excluded (samples E, F and G). The measurements of the powder samples were performed with a PANalytical CubiX^3 diffractometer at the Institute of Geological Sciences, University of Bern. The samples were mixed with corundum as internal standard. The diffractometer was equipped with a Cu source and a secondary beam graphite monochromator. Data were collected from 5 to 60 2Θ with an angular resolution of 0.02 2Θ, 1 s integration time per step, and a fixed divergence slit of 0.25°. Rietveld analyses were performed with Highscore Plus 4.6a from PANalytical.

3.2. Microstructure

3.2.1. Sample preparation

Lineations are not well-developed in the studied rocks, and therefore rock chips for thin sectioning were cut parallel to the general North-directed transport trend in the Flysch. For the high-resolution studies of very fine-grained phases, suitable samples were ion-polished to obtain a smooth surface for high-resolution imaging. We used a slope cutting technique on 5 x 7 x 3 mm large blocks, which were cut from phyllosilicate-rich layers. Cross sections were 1–2 mm^2 in size and were Broad Ion Beam (BIB)-polished from the 7 x 3 mm side with a JEOL SM-09010 BIB argon cross-section polisher (6 kV, 90°, 8 h) at the Geologie-Endogene Dynamik, RWTH Aachen (Klaver et al., 2012).

3.2.2. Microstructural imaging

Thin sections were first studied with a petrographic microscope. In a second step, smaller areas of interest were studied with scanning-electron microscopy (SEM). We used a Zeiss EVO 50 SEM with back-scatter and secondary-electron detectors (BSE, SE) at the Institute of Geological Sciences at the University of Bern. Selected areas of microstructural interest exclude heterogeneities in a similar way as in the XRD analysis (Fig. 2a). The BIB-polished samples were studied with a Zeiss Supra 55 Field Emission SEM with BSE, SE and energy-dispersive spectroscopy (EDS) detectors (Geologie-Endogene Dynamik, RWTH Aachen).

3.2.3. Synchrotron X-ray Fluorescence microscopy (SXFM)

To study the physical and chemical grain-scale processes responsible for foliation formation, we used the XFM beamline at the Australian Synchrotron (Howard et al., 2020). Thin sections with 30 μm thickness were mounted on high-purity quartz slides. We used a horizontal scanning velocity of 2 mm s^{-1} through an 18.5 keV X-ray beam focused to a ~2 μm diameter by a Kirkpatrick-Baez mirror pair. These conditions result in a spatial resolution of ~2 μm with an effective per-pixel dwell of 1 m s. For collection of the excited fluorescence photons, the Maia (Rev D) detector system was positioned in its typical backscatter geometry. All data were analysed using the Dynamic Analysis (Ryan and Jamieson, 1993), as implemented in GeoPIXE (Ryan et al., 2005).

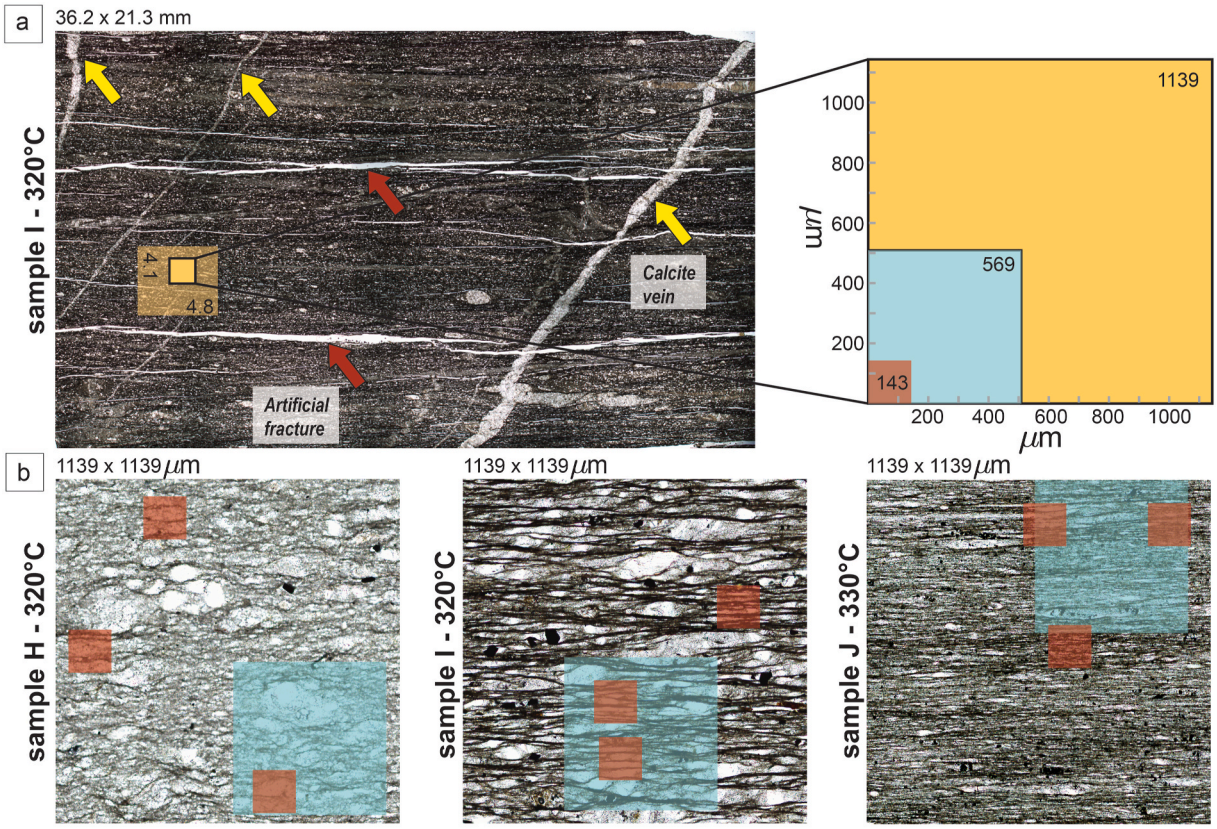

Fig. 2. Workflow showing different selected area sizes for image analysis. a) Photograph of thin section of sample I shows heterogeneity in slate due to veins (yellow arrows), fractures (red arrows) and original sedimentary layering. We selected a homogenous domain and made a mosaic with a petrographic microscope with automatic stage (transparent yellow square), from which we selected a smaller 1139 × 1139 μm tile for ACF analysis in Fig. 5. Within this tile, we selected one area of 569 × 569 μm (blue square) for clast analysis as shown in Fig. 8 and three even smaller tiles per sample of 143 × 143 μm (red square) for foliation analysis as shown in Fig. 7. b) Locations of areas for clast (blue) and foliation (red) analysis indicated for three samples. (For interpretation of the references to colour in this figure legend, the reader is referred to the Web version of this article.)

Table 2
Mineralogical volume% from XRD measurements (<lod = below limit of detection).

	16W01	16SCH01B	16EN1A	17LP06	16MM01	16SP01	16SS01A
Mineralogy	A	B	C	D	H	I	J
Quartz%	13	22	21	19	22	43	17
Calcite%	30	15	21	13	38	9	36
Dolomite%	3	6	6	7	<lod	<lod	<lod
Albite%	5	10	9	13	2	2	<lod
Accessory%	<lod	1	1	1	0	2	2
Phyllosilicate + amorph%	49	46	42	48	38	44	45
Rest%	51	54	58	52	62	56	55

Quantification of all chemical maps was achieved using standard metallic foils.

3.3. Image analysis

3.3.1. Foliation planes

The 2D autocorrelation function (ACF) has become a valuable tool for the statistical and quantitative analysis of spatial patterns in rocks since the pioneering work of Heilbronner (1992). It computes the correlation of a 2D image with itself for the range of all possible lags in the two Cartesian directions x and y, thus producing a 2D map of the autocorrelation coefficient with the same size as the image (Fig. 3). The highest correlation always appears in the centre of the ACF as this represents a 100% correlation of the image with itself. The ACF map reflects the averaged shapes and spatial periodicities of objects in the source image without the need of image segmentation.

Microstructural observations show two main elements making up the slate fabric: clasts and foliation planes. To introduce how these different fabric elements influence the ACF and how they can be interpreted, we first examined a synthetic figure of a circle, representing a clast, and three evenly distributed stripes, reflecting foliation planes (Fig. 3). These ACF figures show that circular objects cause cylindrical ACF patterns, whereas linear objects cause linear ACF patterns. By measuring the distance between the ACF maxima, one can therefore measure foliation distances for linear elements such as foliation spacing.

In this work, we visualise the truncated normalised ACF, either in the interval [0; 0.1] or [0; 0.5]. In this way, more subtle periodic patterns at large lags become visible (Fig. 3). We computed the ACF for plane-polarised-light micrographs. Images for ACF analysis were made with a petrographic microscope equipped with automatic stage under plane-polarised light and 200x magnification (see an overview of original image sizes in Table 3). The bulk ACF is calculated from 1139 × 1139 μm sized images. For all samples, this image width is at least 30 times larger than the characteristic grain width. Hence, each image contains at least a few hundred and up to thousands of grains. In other words, the chosen image size is large enough that grain-scale statistical homogeneity can be assumed. We did not analyse regions with thick fractures, veins, and sedimentary heterogeneity such as interlayering of sandy- and phyllosilicate-rich layers and concentrate on the slate matrix. The selected areas for this study document phyllosilicate-rich layers. From the area of the large 1139 × 1139 μm tile, a smaller one of 569 × 569 μm was selected for clast analysis and a three times smaller tile (143 × 143 μm) for foliation analysis (see Fig. 2a).

From the 2D ACF maps, the foliation distances were measured along manually drawn profiles through the ACF centre (Table 3), which are approximately orthogonal to the periodic ACF line patterns arising from the spatial periodicity of the foliation. As illustrated in the bottom panel of Fig. 3, the mean ACF peak distances along these profiles are an

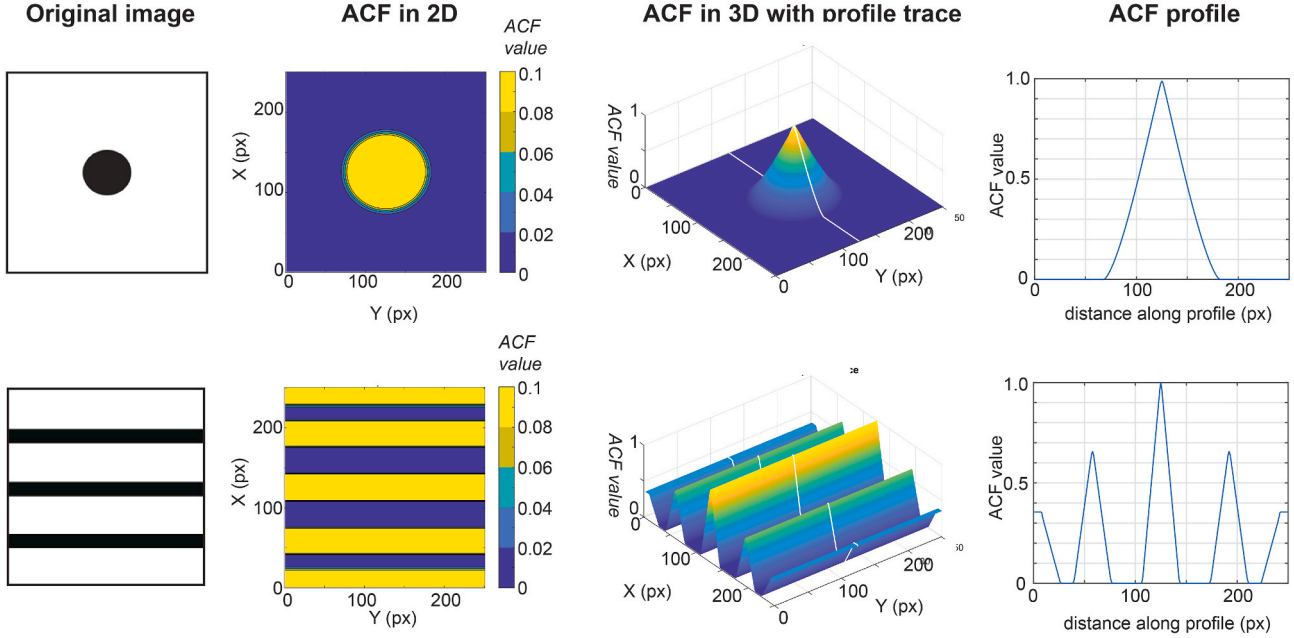

Fig. 3. The autocorrelation function (ACF) applied to two synthetic examples: a single circle and three evenly distributed stripes. In case of the single circle, the ACF is represented by a cylindrical cone, and the ACF profile shows one single correlation maximum in the centre of the image. In case of the stripes, the ACF figure is represented by a wave pattern, and the ACF profile shows several peak maxima. The maxima decrease with increasing distance from the centre of the image. From this synthetic exercise, we observe that circular objects, such as mineral clasts, cause cylindrical ACF patterns whereas linear objects, such as foliation planes, cause linear ACF patterns.

Table 3
Overview of quantitative microstructural analysis. Foliation type after classification from Passchier and Trouw (2005).

Sample label	Peak metamorphic temperature (°C)	Size original image (μm)	ACF size (μm)	Aspect ratio ACF centre (major/minor)	ACF size (μm)	Average foliation distance tile 1 (μm)	Average foliation distance tile 2 (μm)	Average foliation distance tile 3 (μm)	Foliation type
A	200	4269 × 3736	1139 × 1139	1.2	–	–	–	–	Diagenetic
B	230	2747 × 1719	1139 × 1139	1.7	–	–	–	–	Diagenetic
C	230	3246 × 2938	1139 × 1139	2.5	–	–	–	–	Diagenetic
D	250	2729 × 2537	1139 × 1139	4.9	–	–	–	–	Continuous
E	300	4777 × 4547	1139 × 1139	5.4	–	–	–	–	Continuous
F	300	3240 × 2935	1139 × 1139	16.4	143 × 143	35.65	33.77	23.64	Spaced
G	300	4792 × 3716	1139 × 1139	3.5	143 × 143	73.18	45.03	61.92	Continuous
H	320	4284 × 3325	1139 × 1139	4.5	143 × 143	73.18	73.18	46.91	Continuous
I	320	4788 × 4134	1139 × 1139	11.9	143 × 143	20.10	22.52	30.40	Spaced
J	330	5330 × 3303	1139 × 1139	11.5	143 × 143	20.10	18.50	20.10	Spaced

excellent objective measure of foliation spacing. To quantify the elongation of structures, the ACF centre is thresholded at 15%. The long and short principal axis of this segmented central area were measured through fitting the best-fit ellipse, and the corresponding aspect ratio was calculated (Table 3).

3.3.2. Clasts analysis

For clast analysis, outlines of clast grains ($n > 100$) were digitised manually on plane-polarised light micrographs and converted to binary images. The binary images were analysed for area proportion, aspect ratio, grain size, and orientation of the major axis with ImageJ v1.51n (Rueden et al., 2017). The main criterion was that the grains are detrital, excluding any recrystallized or precipitated calcite. Recrystallized calcite was distinguished from detrital calcite clasts by two main criteria: the former is usually located in the pressure shadows around the clasts where it precipitated after dissolution from interfaces with high normal stresses (Wheeler, 1987), and recrystallized calcite is more transparent and fine-grained compared to the whiter and larger detrital grains. The data from this image analysis were further processed with MATLAB (R2017b) to obtain clast statistics from aspect ratio, orientation of the major axis and distributions of area-weighted grain size frequencies (Berger et al., 2011).

3.3.3. Phase segmentation

The basis for phase segmentation are the BIB-SEM images. In a first step, individual phases in the BSE image map were segmented through grey-level slicing and transformed into a binary image. For filtering out phases with overlapping greyscale levels, e.g., to separate dolomite from calcite and albite from quartz, we used EDS maps. Finally, all the maps were cleaned manually for artefacts, and some grains that could not be segmented with thresholding were drawn manually.

4. Results

4.1. Macroscopic field observations

The sedimentary sequences in the field consist of slate layers alternating with marl, carbonate, sandstone and quartzite layers. The main schistosity (S1) dips towards the SSE with an average dip direction/dip of 160/60 (Akker, 2020). In most cases, the schistosity makes a very small angle with the bedding. Folds occur mostly locally and show a well-developed axial plane cleavage, which, in some cases, is filled in by younger vein generations. Slate-dominated sequences occur mostly in the northern part of the field area throughout the different Flysch units between Weesen and Nideren (Fig. 1). South of Nideren, the slates are more frequently interlayered with carbonates and sandstones. For this study, we only examined hand specimens from slates, excluding as much as possible any other lithologies, over a north-south transect covering a metamorphic gradient from 200 °C to 330 °C (Fig. 1). Locally, vein-arrays of a few metres wide occur in the slate layers and are characterised by a high spatial concentration of foliation-parallel calcite and calcite-quartz veins. The slates around these veins show an intense foliation macroscopically as well as characteristic preferential weathering, often leading to topographic depressions.

4.2. Microscopic microstructures and mineralogy

According to XRD, the main mineralogy of the slates comprises quartz, calcite, white mica, and chlorite. Dolomite, albite, siderite, pyrite and rutile are minor phases. The volume proportions of phyllosilicates vary between 38% and 49% with an average of 45% (Table 2: sample A to J). Volume proportions of quartz range from 13% to 22% with an average of 19%. An additional sample (sample I) with a quartz proportion of 43% is an outlier because of numerous quartz micro-veins (Fig. 2a). The volume proportions of calcite vary from 9% to 38%, with an average of 23%. This considerable variability allows us to study the effect of calcite on the microfabric. We selected two calcite-rich samples at two end-member temperatures at 200 °C and 320 °C (sample A and H, Fig. 4a and b). Both samples contain fossils in an originally mud-rich matrix. In the case of the low-temperature sample, the matrix shows a very weak fabric with poorly aligned detrital phyllosilicates with lengths of tens of micrometres. In contrast, the high-temperature sample contains well-developed anastomosing pressure solution seams containing secondary phyllosilicates with lengths <10 μm. We compare these two samples with two samples with lower amounts of calcite and higher amounts of quartz (sample C and I) that also experienced two different peak metamorphic temperatures (230 °C and 320 °C, respectively; Fig. 4c and d). The low-temperature quartz-rich sample shows isolated phyllosilicates with a strong shape-preferred orientation (SPO) in a fine-grained matrix where anisotropic detrital clasts also exhibit a clear SPO. At higher temperature, the quartz-rich sample shows a well-developed parallel dissolution foliation alternating with well-aligned, highly stretched microlithons.

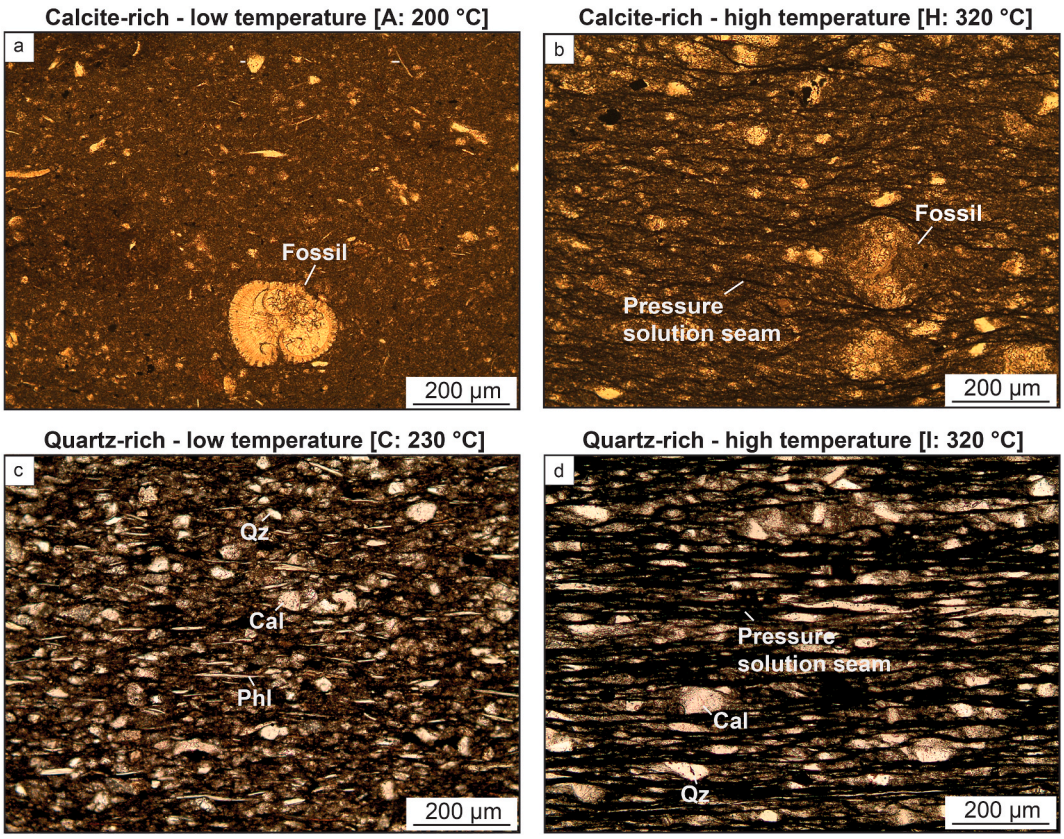

Fig. 4. Photographs showing the effect of composition and temperature on the microstructure as seen in thin sections. a-b) Calcite-rich slate compared at low and high metamorphic temperature. At low temperature (a) the fabric is weakly deformed. At high temperature (b) pressure solution seams, mostly wrapping around the fossil clasts, make up an anastomosing foliation fabric. c-d) Quartz-rich slate samples compared at low and high metamorphic temperature. At low temperature (c) phyllosilicates are aligned. At high temperature (d) pressure solution seams are parallel and make up the parallel foliation fabric. Samples: (a) Sample A, (b) Sample H, (c) Sample C, (d) Sample I.

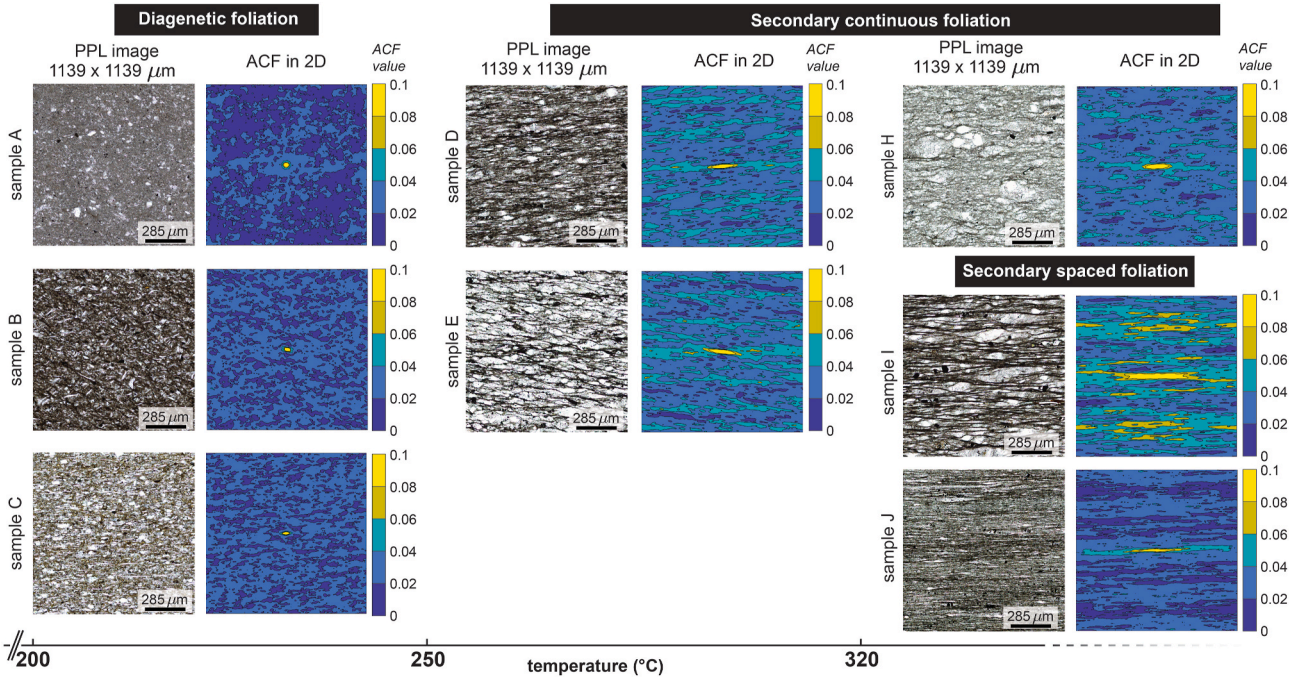

Fig. 5. ACF figures calculated in 2D for plane polarised light (PPL) photographs of samples along the metamorphic gradient. Bedding orientation is always horizontal. Three groups of deformation fabrics can be recognized: i) diagenetic foliation defined at temperatures between 200 and 250 °C, ii) secondary continuous foliation at temperatures between 250 and 320 °C and iii) a continuous foliation as well as a secondary spaced foliation at temperatures of 320–330 °C. See text for explanation of the ACF figures.

4.3. Fabric evolution along the metamorphic gradient

The microstructural evolution along the metamorphic gradient from 200 °C to 330 °C is documented with the use of the ACF (Fig. 5). Along the metamorphic gradient, we distinguish three microstructural end-member stages. For the description of foliations, we employ the classification of Passchier and Trouw (2005). In this classification scheme, diagenetic foliations are separated from secondary foliations. Diagenetic foliations are the result of diagenetic compaction in un- or weakly consolidated sediments and are bedding-parallel due to passive rotation of the phyllosilicates. However, the fabric elements show very little elongation, and the ACF centre is therefore round shaped. Secondary foliations form after lithification as the result of deformation and metamorphism and comprise a large variation in morphological features. These fabric elements include a higher amount of elongated structures than the ones in the diagenetic fabrics and show therefore a rather elongated ACF centre (high aspect ratio). According to this classification scheme, we classify our rocks into three groups of foliations: diagenetic foliations, secondary continuous foliations, and secondary spaced foliations. Secondary continuous foliations still contain unconnected foliation domains while secondary spaced foliations feature interconnected foliation domains.

4.3.1. Stage i: diagenetic foliation

The samples at lowest metamorphic peak temperatures, between 200 °C and 230 °C, show a fabric dominated by low-aspect ratio clasts

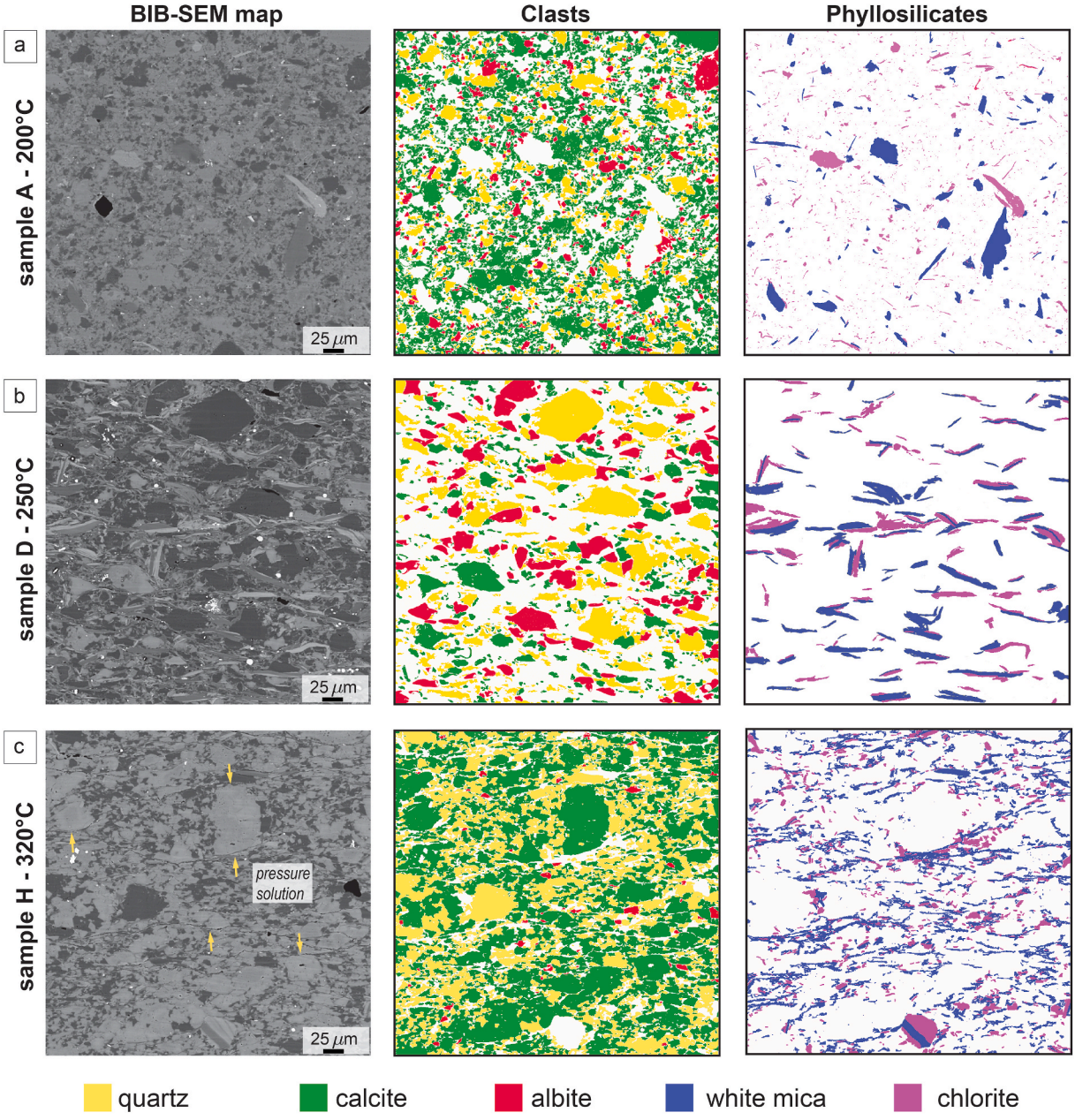

Fig. 6. Result of phase segmentation on BIB-SEM BSE images for three samples along the metamorphic gradient. Clasts are separated from phyllosilicates. a) Sample A shows a fabric closest to that expected for the initial weakly deformed sediment. Phyllosilicates in the slate matrix of this sample are mostly randomly oriented. b) In sample D, both clast and phyllosilicate sizes are relatively larger than in sample A. The diagenetic fabric is defined by an alignment of phyllosilicates. c) The clast sizes in sample H are similar as in sample D, but the phyllosilicate grain sizes are reduced. The small phyllosilicates start to form interconnected networks and form the continuous foliation as defined in Fig. 5. Note: for samples with a secondary spaced foliation such phase segmentation could not be performed due to the fine grain sizes and resolution limit. To investigate foliation formation in these samples, SXFM maps are employed in Fig. 9.

and a very weak alignment of phyllosilicates (left panel in Fig. 5). The aspect ratio of the segmented ACF centres varies from sample A to C from 1.2 to 2.5 (Table 3). In the following, we consider ACF centres with aspect ratio = 3 as the threshold value for the transition from a diagenetic foliation (aspect ratio < 3) to a secondary foliation (aspect ratio ≥ 3). In sample A, the long-axis orientation distribution of ACF centres is random, indicating an isotropic fabric. Sample B shows the formation of a foliation slightly oblique to bedding while sample C demonstrates a clear bedding-parallel fabric. However, the aligned phyllosilicates in these three samples are spatially unconnected (Fig. 5). This is confirmed by the phase segmentation map of sample A (Fig. 6a), which shows that this calcite-rich sample is matrix-supported by rounded calcite clasts. The phyllosilicates do not show a SPO.

4.3.2. Stage ii: secondary continuous foliation

At intermediate peak metamorphic temperatures (250 °C–300 °C), the microstructures are defined by a stronger SPO of phyllosilicates than observed in samples with a diagenetic foliation. This is demonstrated by more elongated ACF centres with aspect ratio between 3.5 and 5.4 (Table 3, central panel of Fig. 5). In addition, the phyllosilicates form interconnected foliation seams, which, in some cases, are anastomosing (see samples E and H in Fig. 5). Foliation spacing ranges from 45 to 73 μm (Fig. 7, Table 3). The clast-supported sample H (25% of the total measured area comprises clasts) consists of relatively large rounded clasts, which exhibit two main orientations of their long axes, confirming the anastomosing nature of the foliation (sample H, Fig. 8a). The evolution of a continuous foliation is also nicely demonstrated in the phase segmentation map of sample D (250 °C) and H (320 °C) (Fig. 6b and c). Compared to sample A (Fig. 6a), the clasts in sample D and H appear more elongated. The relatively coarse-grained phyllosilicates in sample D are aligned and sometimes interconnected, forming the continuous foliation fabric. In sample H, the clast surfaces (mostly calcite) perpendicular to the main flattening direction are truncated (Fig. 6c). Such surfaces are typically affected by pressure solution. The fine-grained phyllosilicates form interconnected networks and follow the clast shapes (Fig. 6c).

4.3.3. Stage ii: secondary spaced foliation

The samples at highest metamorphic temperature around 320 °C–330 °C show an even stronger anisotropic fabric (Fig. 5), forming a smooth spaced foliation with a volume fraction of 50–70% of foliation domains. The segmented ACF centres have aspect ratio of 11.5 and 11.9, indicating high elongation. Such a high aspect ratio is also seen in the slate associated with a vein-array (sample F). The ACF figure of the samples with a spaced foliation shows a well-developed fabric of interconnected phyllosilicates forming a parallel foliation. The foliation

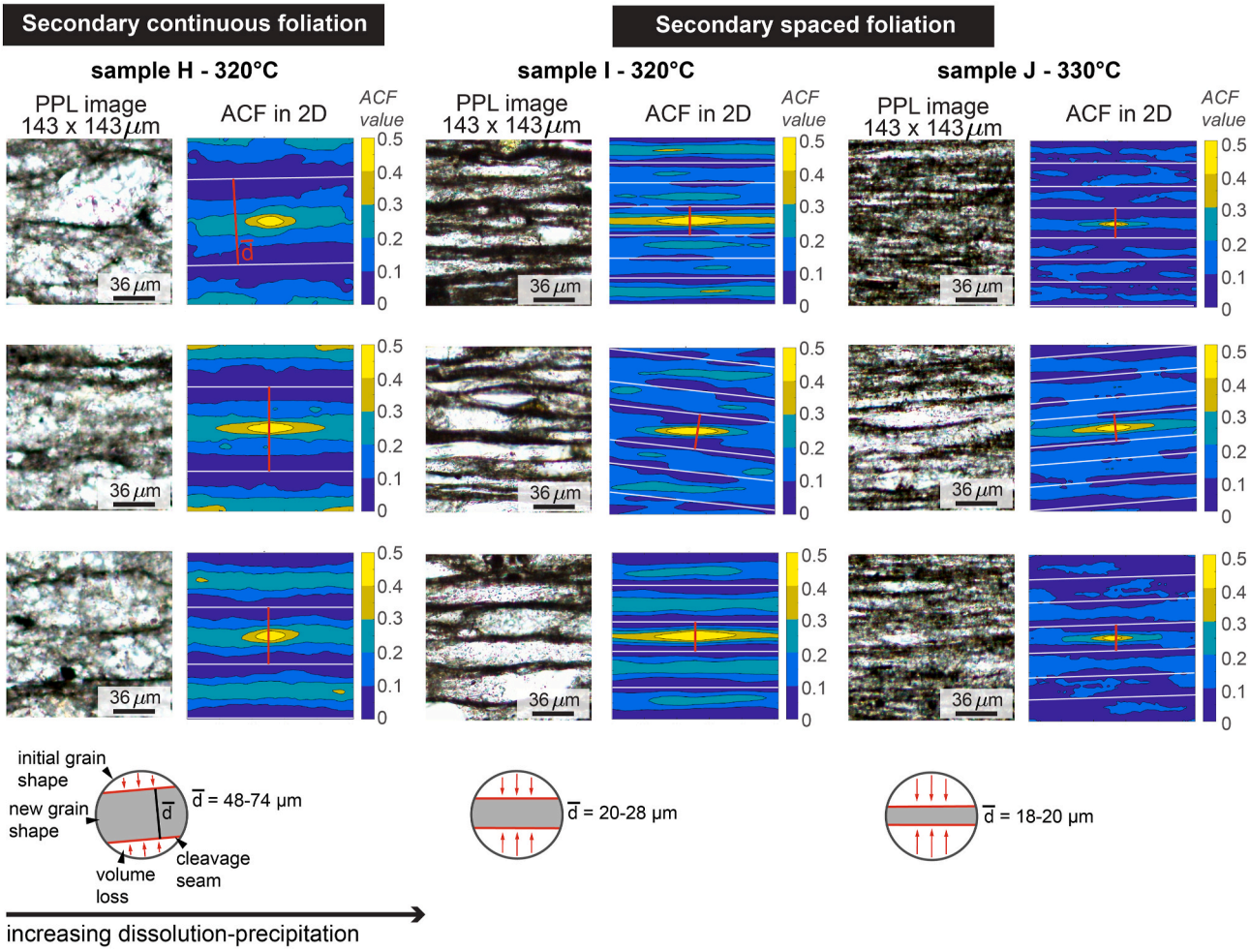

Fig. 7. Three foliation domains from three different samples, captured in plane polarised light photographs (PPL) and calculated with ACF in 2D. In sample H, varying clast sizes and shapes result in a secondary continuous foliation. This is reflected by a relatively larger variation in foliation spacing ($\overline{d}$, red lines, note: only one red line is shown per ACF figure. See overview of all measured foliation distances in Table 3). The foliation domains become more regular and parallel in samples I and J, where clasts are more elongated. In these samples, the foliation spacing is significantly reduced compared to sample H. This is also indicated in the schematic drawings, where increasing pressure solution reduces and changes the grain shape, resulting in a decrease in $\overline{d}$ for samples with a secondary spaced foliation. (For interpretation of the references to colour in this figure legend, the reader is referred to the Web version of this article.)

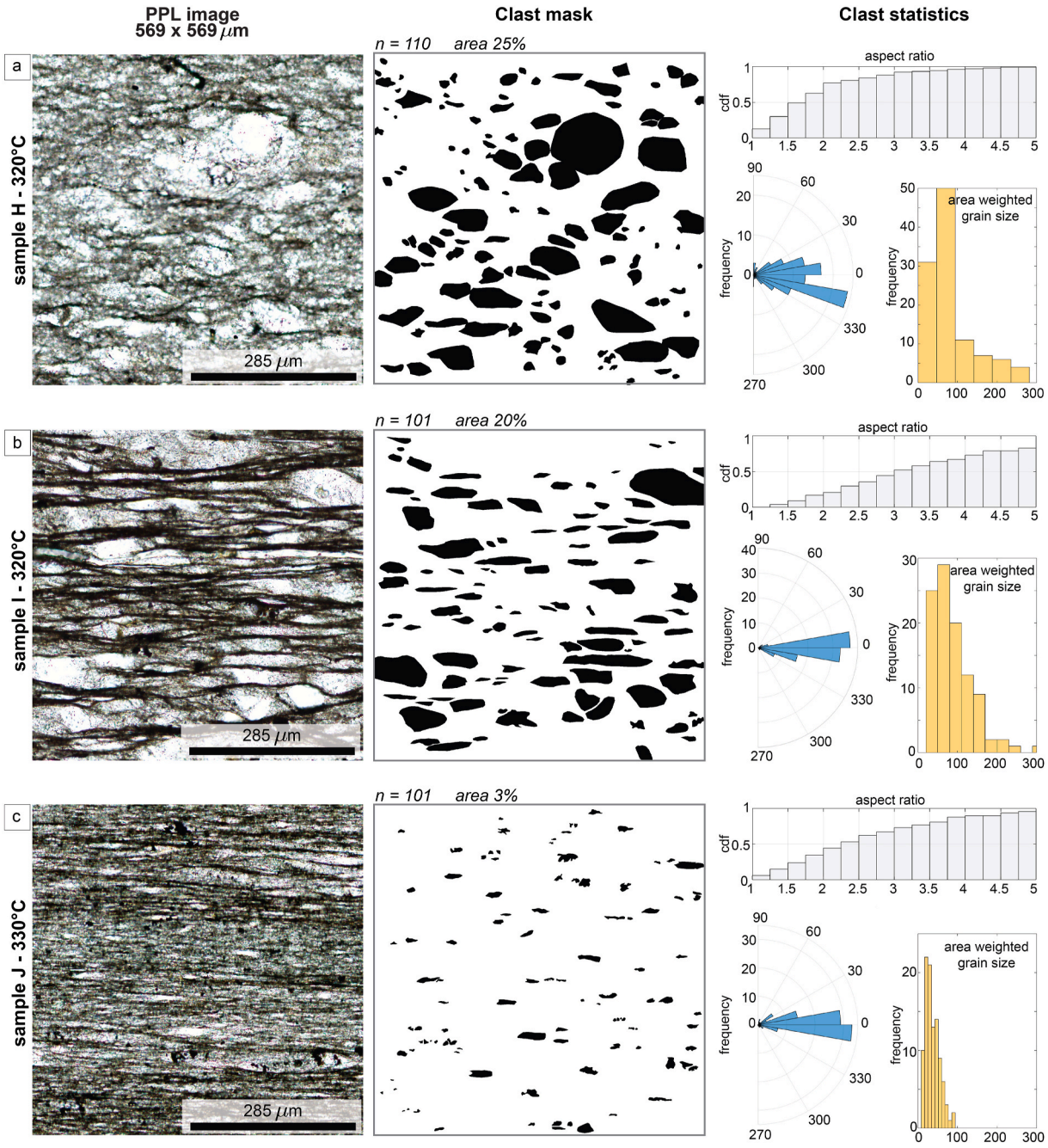

Fig. 8. Clasts (quartz, calcite, dolomite, albite) analysis from three samples along the metamorphic gradient. Left column: plane polarised light (PPL) photographs. Middle column: clast masks indicate area % of clasts. Right column: histograms of aspect ratio of clasts show that in sample H (secondary continuous foliation) grains are more rounded than in sample I and sample J (secondary spaced foliation). The area weighted grain size distributions show that grain size is smallest in sample J, which shows a dense secondary spaced foliation. The rose diagrams indicate most spread in major axis orientation for sample H, which agrees with the anastomosing foliation fabric of that sample. Therefore, anisotropy is highest for sample I and J, which both have a secondary spaced foliation.

spacing is 19–20 μm in the case of sample J (Fig. 7). The area proportion of clasts is reduced to 3% (Fig. 8c). Geometric statistics show a reduction in grain size and increase in aspect ratio of clasts (Fig. 8c). For samples with this type of foliation, we were not able to obtain SEM-based phase segmentation maps due to the strong grain size reduction. However, SXFM maps, especially the ones showing Ti and Rb concentrations, confirm the alignment of phyllosilicates in narrowly spaced and bedding-parallel foliation planes (Fig. 9).

5. Discussion

Our data indicate first-order variations in microfabric development in slates related to changes in metamorphic conditions from the outer to the inner wedge (i.e., metamorphic increase from north to south). In the following, we discuss the physical and chemical deformation mechanisms on the grain-scale as a function of their thermal activation with increasing metamorphic conditions and investigate how deformation expressed on the wedge-scale is accommodated by grain-scale deformation. Despite the long lasting deformation history of the study area, all foliation-forming processes must have occurred before the peak-to

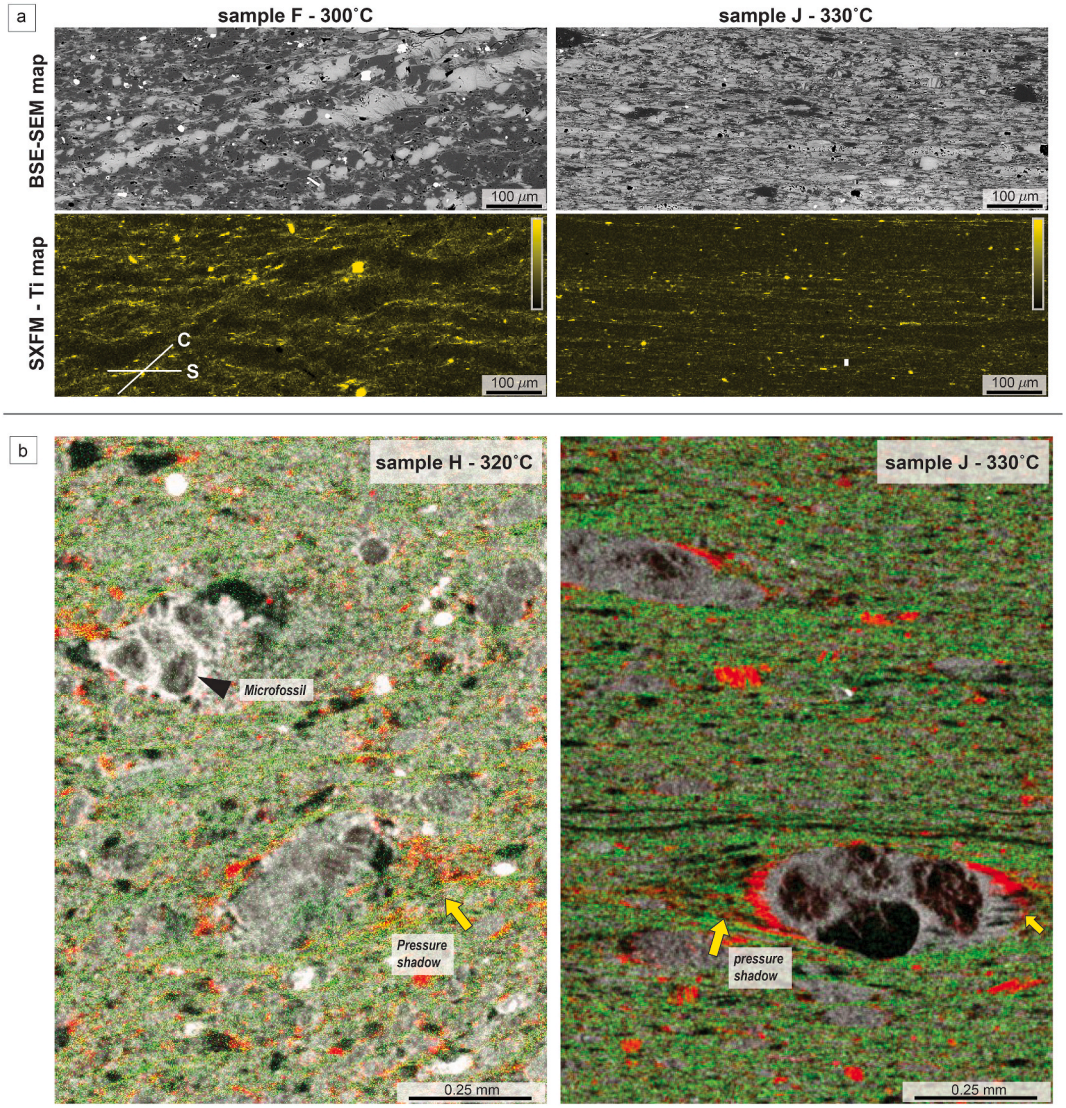

Fig. 9. BSE-SEM and SXFM maps from different samples. a) SXFM-Ti maps show an anastomosing network of phyllosilicates for sample F, and a rather parallel foliation fabric for sample J. Black to yellow: low to high Ti concentration. **b)** These are composite SXFM maps: Fe = red, Rb = green, Sr = grey. The microfabric of sample H, shows round microfossils with pressure shadows filled with chlorite (high Fe concentrations) and other phyllosilicates (high Rb concentrations). The overall fabric is classified as a continuous foliation. Sample J also shows microfossils with pressure shadows. However, here the microfossils are more elongated, and the foliation is increasingly dense, showing a well-developed spaced foliation. (For interpretation of the references to colour in this figure legend, the reader is referred to the Web version of this article.)

retrograde metamorphic activity of the out-of-sequence thrusting of the Glarus thrust (Calanda-/Ruchi Phase of Milnes and Pfiffner (1977), since the main foliation is sheared into the thrust plane (Ebert et al., 2007; Herwegh et al., 2008). In this light, all microphysical deformation processes within the paleo-wedge described below account for deformation on the prograde metamorphic path of an accretionary wedge.

5.1. *Microstructural evolution of clasts and secondary foliations*

The shallow part of the accretionary wedge, the outer wedge, is characterised by fold-and-thrust structures accommodating substantial horizontal shortening (Dielforder et., 2016a; Ditullio and Byrne, 1990; Moore et al., 1990; Raimbourg et al., 2009). The horizontal shortening causes dewatering and ductile strain in the sediments, which show typically stratal disruption, folding and compaction bands (e.g., Dielforder et., 2016a; Elphick et al., 2021; Fagereng et al., 2019; Morgan and Karig, 1995; Orange et al., 1993; Sample and Moore, 1987; Vannucchi and Bettelli, 2002). The soft-sediment deformation in this domain is mostly accommodated by particulate flow due to grain boundary sliding and grain rotations (Dielforder et., 2016a; Fagereng et al., 2019; Morgan and Karig, 1995). Particulate flow also involves intragranular deformation to a certain degree and is a function of pore-fluid pressure (Borradaile, 1981; Maltman, 2012). In contrast, sediments in the inner wedge are typically well-lithified and characterised by pressure solution, cementation, and veining (e.g., Dielforder et., 2016a; Palazzin et al., 2016; Sample and Moore, 1987). In the following, we focus on the evolution of the microstructural gradient in the inner wedge.

5.1.1. *Systematic changes in clast aspect ratio and foliation geometry along the metamorphic gradient*

The investigated microstructures along the metamorphic gradient in this study all show deformation structures (pressure solution seams (Figs. 4 and 9), veining (Fig. 2a)) typical for the well-lithified sediments in the inner wedge. The microfabric of these slates at the lowest investigated temperature T = 200 °C is defined by weakly aligned phyllosilicates without major SPO. This fabric is interpreted as diagenetic foliation (Passchier and Trouw,

2005) (Figs. 5 and 6a). All the studied samples subjected to higher metamorphic grade (>250 °C) show a steeply dipping secondary foliation, made up of interconnected phyllosilicates with a strong SPO (Figs. 5 and 6), in line with microstructural observations made in turbidites of various accretionary complexes (e.g., Raimbourg et al., 2009). In most cases, the secondary foliation is parallel to the primary foliation (bedding) because of the regional deformation-induced large-scale tight to isoclinal folding and associated formation of an axial planar foliation, which often appears as transposed composite foliation (Gasser and Den Brok, 2008). The secondary foliation evolves generally from a continuous foliation at temperatures around 250 °C–320 °C (Fig. 5) to a spaced foliation at temperatures >320 °C (Fig. 5). The evolution of the microfabric is characterised by quantifying fabric intensity as proxy for finite strain and foliation spacing with the use of the ACF. The increase in aspect ratio of the central ACF peak along the metamorphic gradient from north to south is shown by the following statistical analysis (Table 3 and Fig. 10). We calculated Spearman's rank correlation coefficient ρ for aspect ratio and temperature, which quantifies if two datasets can be described by a monotonous (linear or non-linear) correlation. We obtain $\rho = 0.74$ for the whole dataset in Table 3, with a p-value of 0.007 for the null hypothesis that temperature and aspect ratio are not correlated positively (Fig. 10a). Hence, despite the significant spread of the data, there is great statistical confidence that temperature correlates positively with the fabric aspect ratio. The secondary foliation spacing decreases from about 60 μm for continuous foliation fabrics at intermediate temperatures, down to 20 μm for spaced foliation fabrics at high temperatures (Table 3). Examining the whole foliation spacing dataset (Table 3, Fig. 10a) for a negative correlation with temperature gives $\rho = -0.55$ with a p-value of 0.017 for the equivalent null hypothesis. This correlation strengthens when only considering spaced foliations, yielding $\rho = -0.86$ with $p = 0.004$. Hence, there is reasonable statistical confidence that foliation spacing decreases as temperature increases.

So why is there considerable scatter in our data, both for aspect ratio and foliation spacing? First, our statistical analyses neglect the uncertainty of the natural temperature estimates which are on the order of 10 °C (Ebert et al., 2007). Second, on the grain-scale, clast aspect ratios and the morphology and spacing of foliation are strongly controlled by compositional heterogeneity, the microfabric of the sedimentary protolith, and the related deformation mechanisms, which vary from sample to sample and are determined by the sedimentary protolith (Alvarez et al., 1978; Engelder and Marshak, 1985; Gratier et al., 2013a; Gratier, 1987; Marshak and Engelder, 1985; Railsback, 1993). Since the tectono-metamorphic overprint in most samples is high and clearly involves material loss, grain-size changes, and re-as well as neo-crystallization, we cannot determine the original protolith properties with any confidence. Finally, differences in finite strain are also expected to contribute to the scatter (Alvarez et al., 1978; Gratier, 1987; Rutter, 1976), yet another quantity, which is notoriously difficult to measure in highly transposed slates. However, our data show clearly that the volumetrically most important deformation mechanism is pressure-dissolution-precipitation creep at T > 230 °C (Figs. 8 and 9), as observed in other slates (Roo, 1989; Sorby, 1853; Waldron and Sandiford, 1988; Wright and Platt, 1982) and discussed further below. This deformation mechanism can be divided into three subsequent, potentially rate-limiting steps: dissolution, transport, and precipitation (Gratier et al., 2013a). A comprehensive review is beyond the scope of this paper and can be found in Gratier et al. (2013a). Considering the fundamental physical relationships underpinning pressure-dissolution-precipitation creep, it becomes clear that, in most cases, the relevant thermodynamic forces (potential differences) are proportional to the product of the universal gas constant R and temperature (Gratier et al., 2013b). In other words, an increase in temperature is generally expected to promote pressure-dissolution-precipitation creep under the prograde metamorphic conditions the study area experienced. We interpret the statistically meaningful correlations between aspect ratio or foliation spacing and temperature as a reflection of this physical relationship.

5.1.2. *The effects of protolith heterogeneity*

Although we sampled only slate-rich layers, microstructural observations reveal large mineralogical and geometric heterogeneity on the thin-section scale, which certainly reflect differences in the sedimentary protoliths and probably finite strain (Gratier, 1987; Rutter, 1976). The slates contain alternating calcite-, phyllosilicate-, and quartz-rich layers of about 100 μm in width. We compared micro-layers of various composition along the temperature gradient to study the effect of composition on the evolution of microfabrics and deformation processes. A comparison of low- and high-temperature examples of calcite-rich and quartz-rich layers reveals composition- and fabric-specific microstructures (Fig. 4). The calcite-rich sample A at low temperature (Fig. 4a) shows large rounded microfossils (*Globigerina* sp.) embedded in a fine-grained matrix of phyllosilicates, calcite, and quartz without any obvious secondary foliation. The equivalent high-temperature example (sample H, Fig. 4b) contains a penetrative, interconnected, secondary continuous foliation that anastomoses around the large rounded but elongated fossil clasts. In contrast, the quartz-rich sample C already exhibits a weak fabric of aligned phyllosilicates at low temperature (Fig. 4c). Its high-temperature equivalent sample I (Fig. 4d) features a penetrative, interconnected, narrow, planar, spaced foliation. These observations indicate that the initial sedimentary fabric plays an important role in the formation of the finite metamorphic foliation. It appears probable that the initial density and grain-size distribution of clasts has a major influence on foliation development (Engelder and Marshak, 1985; Gratier et al., 2013a; Gratier, 1987; Railsback, 1993).

Samples A and C may represent two geometric end-members. Sample A has a matrix-supported microfabric with a bimodal clast-size distribution (comparatively large foraminifera and smaller detrital as well as other fossil clasts) while sample C exhibits a grain-supported microfabric with relatively equant quartz and calcite detrital clasts. In the former case, pressure dissolution probably commenced in a distributed fashion in the micro-to nano-granular matrix, as seen in, for example, the compaction of wackestones (Shinn and Robbin, 1983). The large fossil clasts were likely more resistant to dissolution than smaller detrital clasts and the matrix because of their internal microfabric and monomineralic nature (Gratier et al., 2013a; van den

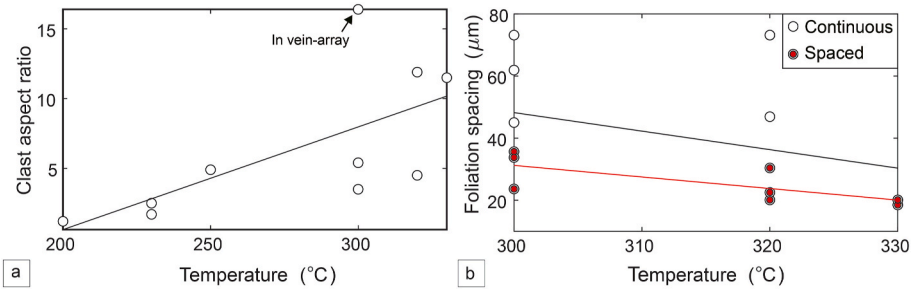

Fig. 10. Fit statistics for aspect ratio of analysed fabrics and foliation spacing as function of peak metamorphic temperature show that both correlate with peak metamorphic temperature with high confidence.

Ende et al., 2019). With increasing strain and time, the clast spacing decreased as the matrix compacted and dissolved. Nascent dissolution seams would have been arrested at the boundaries of poorly soluble large clasts, laying the foundation for the anastomosing geometry of the foliation seen at high temperature. Once clast packing reached the point of a grain-supported fabric, increasing contact stresses at clast-clast interfaces could have promoted dissolution further (Wheeler, 1987), leading to the well-developed anastomosing foliation seen in Fig. 4b. In the other end-member (sample C, Fig. 4c), pressure dissolution evidently commenced when the rock already had a grain-supported fabric including fine-grained phyllosilicates with a SPO. Both factors – high contact stresses and phyllosilicates at clast interfaces – promote the formation of dissolution seams, as outlined in detail by Nenna and Aydin (2011). In summary, these observations support the notion that the protolith fabric has a significant impact on the formation of secondary foliations through pressure-dissolution-precipitation creep (Passchier and Trouw, 2005; Roo, 1989; Sorby, 1853; Waldron and Sandiford, 1988; Wright and Platt, 1982).

5.2. Deformation mechanisms on the grain scale

The alignment necessary for the development of the foliation made up by the SPO of phyllosilicates requires either: i) deformation-induced rotations, such as described in Etheridge and Hobbs (1974); Gray (1978); Groshong Jr (1988); Herwegh and Jenni (2001); White and Knipe (1978), ii) re- and neocrystallization, for example caused by pressure solution (e.g., Bons, 1988; Bos and Spiers, 2002; Cosgrove, 1976; Durney, 1972a; Durney, 1972b; Marlow and Etheridge, 1977) or, iii) a combination of these two processes (e.g., Herwegh and Jenni, 2001; Ho et al., 1996; Ishii, 1988; Oertel, 1983). The driving force for rotation is deformation, which in the case of the inner wedge is a combination of vertical loading and horizontal shortening. In addition to tectonic forcing, re- and neocrystallization requires chemical processes such as dissolution-precipitation and mass transfer (Bos and Spiers, 2002; Rutter, 1983), and thus coupled physical-chemical processes are responsible for the necessary grain alignments.

5.2.1. Evidence for deformation-induced rotations

The sedimentary protoliths of the investigated Flysch units contain grains with low aspect ratios (quartz, calcite, feldspar, fossils) and platy grains with high aspect ratios (phyllosilicates). If not already preferentially oriented during sedimentation, the anisotropic phyllosilicate platelets reorient during burial diagenesis and subsequent deformation. Hence, only original detrital grains can be used as indicators for such rotations. For example, large detrital phyllosilicate grains of mixed aggregates (chlorite-white mica) are folded, rotated, and kinked and are not aligned with the foliation (Fig. 11a), indicating large deformation-induced rotations in the studied slates. However, as indicated by K–Ar analytics in combination with microstructural analyses, Akker et al. (2021) showed that at $T > 250$ °C, most phyllosilicates are secondary and aligned with the foliation because they formed during synkinematic pressure-dissolution-precipitation creep.

5.2.2. From source to sink: tracking material fluxes during foliation development by pressure-dissolution-precipitation creep

On the grain-scale, dissolution is coupled to mass transport and precipitation as material is moved from the sources to the sinks (e.g., Durney, 1976; van der Pluijm et al., 1998). Pressure solution results in an elongation of clasts (Durney, 1976; Wenk et al., 2019), which accompanies the development of microlithons, a decrease in foliation spacing, and a reduction in grain size (sample I and J: Figs. 7 and 8). The change in shape indicates that the clasts are source sites for mass removal by pressure solution, a process whose efficiency increases with

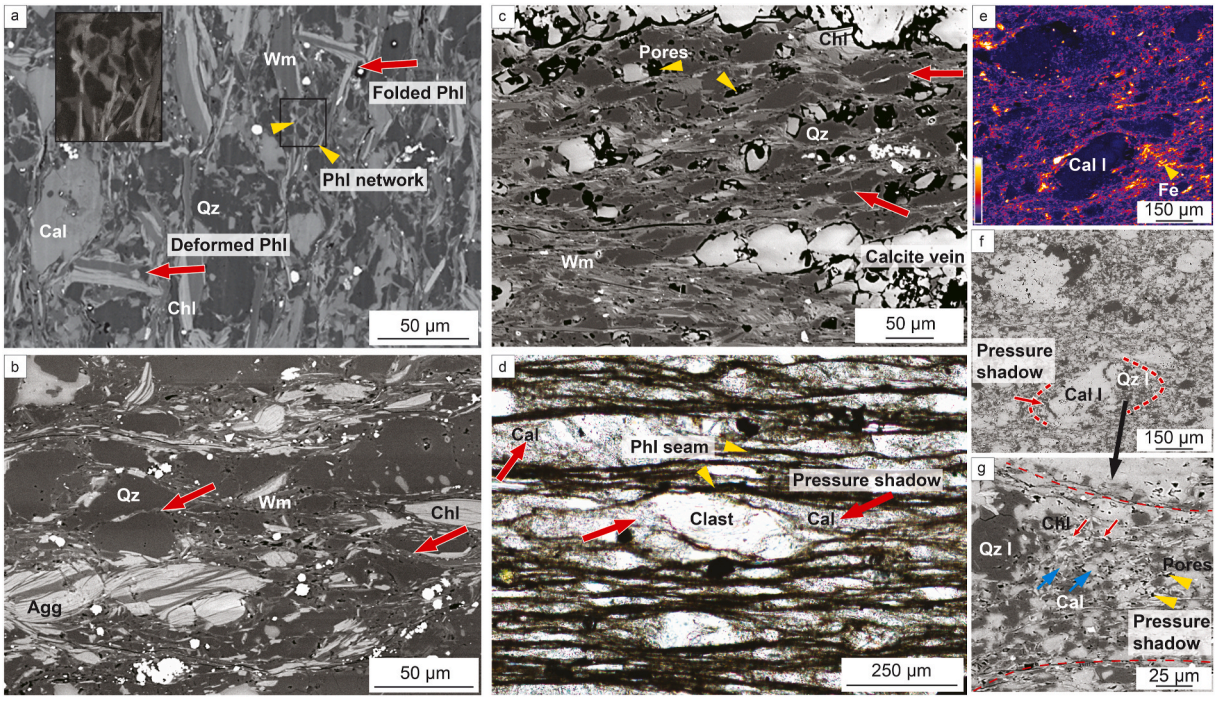

Fig. 11. Grain-scale processes of the formation of foliation in slates. a) Phyllosilicates are folded and deformed (red arrows) indicating physical grain rotation processes. Some small phyllosilicates precipitate and form networks as they wrap around quartz and calcite clasts (see zoom in upper left corner). b) Phyllosilicates precipitate around dissolved and fractured quartz grain boundaries (red arrows). c) Quartz aggregates are heavily fractured (red arrows), phyllosilicates precipitate in networks. The zone contains a calcite vein and is highly porous. d) Calcite precipitates in pressure shadows of clasts forming layers. e) SXFM-Fe map of the area in (f) shows the precipitation of chlorite in a pressure shadow by elevated Fe concentrations. f) Polymineralic mixtures precipitate in pressure shadows around calcite clasts g) Zoom in of (f) shows that the polymineralic mixture in the pressure shadow is made up of quartz, white mica, calcite (blue arrows), chlorite (red arrows) and shows the formation of numerous pores (yellow arrows). (For interpretation of the references to colour in this figure legend, the reader is referred to the Web version of this article.)

metamorphic temperature (Gratier et al., 2013a). This is also demonstrated by the aforementioned increasing ACF aspect ratio of the fabric and the decreasing foliation spacing (Fig. 10).

Such shape changes of detrital clasts could also result from grain-internal deformation by crystal-plastic deformation mechanisms. In the case of crystal-plastic processes such as dislocation creep, the shapes of deformed clasts embedded in a viscous matrix are sometimes interpreted in terms of the minimum finite strain (e.g. Bouchez (1977); Jeffery (1922); March (1932); Schrank et al. (2015). However, if elastic and plastic contributions to the bulk rheology become important (in a continuum-mechanical sense), it becomes difficult to use the shapes of crystal-plastically deformed strong clasts as strain gauges (Schrank et al., 2015). In our samples, the lack of subgrains and undulose extinction indicate that dislocation creep did not operate in any of the present minerals (calcite, quartz, feldspar, phyllosilicates). In addition, elongated clasts from former *Globigerina* sp. fossils with marked neo-crystallization in their pressure shadows retain the circular shape of their internal chambers, even in highly deformed samples with well-developed spaced foliations (Fig. 9b). This indicates absence of internal viscoplastic deformation due to crystal plasticity.

The sinks are precipitation sites for authigenic phyllosilicates, calcite, and quartz. Sites for calcite and quartz precipitation must be either in the microlithons or, more likely, in calcite and quartz-calcite veins (Figs. 2a and 11c), which continuously form during the entire deformation sequence from outer to inner wedge (Dielforder et., 2016a; Dielforder et al., 2015). In terms of sinks being indicative of phyllosilicate mass transfer, we discern three different precipitation sites: (i) pressure shadows of strong, poorly soluble clasts, (ii) along grain boundaries, and (iii) on foliation planes. All these sites are important in order to understand why, how, and where the overall foliation structures evolve.

(i) Most obvious at first glance is precipitation in pressure shadows around fossils, which are filled with recrystallized calcite in some cases (Fig. 11d). This process causes elongation of clasts and potentially contributes to the formation of microlithons (Fig. 11d). In other places, pressure shadows are filled with polyphase mixtures of calcite, quartz and phyllosilicates (Fig. 11e,f,g). In such cases, the polyphase mixture in the pressure shadow is often characterised by an elevated microporosity (Fig. 11g).

(ii) Inter- or transgranular fractures constitute a second sink for the precipitation of phyllosilicates. They are particularly common in quartz-rich grains and layers (Fig. 11b and c), and the associated dilation is an effective process to create sites for precipitation of phyllosilicates. This also helps to form interconnected phyllosilicate layers, particularly within microlithons. Fracture-hosted phyllosilicate precipitates are often at high angles to the main foliation and link foliation-parallel phyllosilicate seams across the branches of the main foliation. Consequently, main and subsidiary oblique phyllosilicate seams wrap around clasts and microlithons, resulting in the anastomosing fabrics in the continuous foliation domains.

(iii) The most important precipitation sites are the main foliation planes. In the past, these sites have preferentially been interpreted to mainly form by passive accumulation of non-soluble phyllosilicates, while other matrix minerals such as quartz, feldspars or calcite were dissolved away and therefore depleted (e.g., Durney, 1972a; Heald, 1955; Weyl, 1959). The platy shape of phyllosilicates favour dissolution of neighbouring quartz, feldspar and calcite grains (e.g., Durney, 1972a; Heald, 1955; Weyl, 1959), particularly in the case of stress concentrations along grain interfaces (e.g., Bos et al., 2000; Bos and Spiers, 2001; Bos and Spiers, 2002; de Meer et al., 2002; Niemeijer and Spiers, 2005; Wheeler, 1987). The foliation planes of the studied slates are enriched in relatively insoluble Ti (Figs. 9a and 12b), suggesting that these are sites of dissolution. However, the foliation planes are also enriched in Rb, which is usually hosted by phyllosilicates (Figs. 9b and 12d), and could be explained by passive accumulation of insoluble detrital phyllosilicates, neocrystallization of new (authigenic) phyllosilicates, or a combination of both processes. Unequivocal detrital micas in our high-temperature samples usually consist of white mica-chlorite intergrown assemblages (Fig. 12). The grain boundaries of the few remaining large detrital mica clasts show clear evidence of dissolution. Moreover, the Rb-distribution within the very fine-grained foliation planes is fairly homogeneous and consistently lower compared to the localized, elevated Rb concentrations in detrital phyllosilicates (Fig. 12d). Therefore, the fine-grained phyllosilicates making up the foliation planes are most likely authigenic. More evidence for phyllosilicate re- and neocrystallization are changes in phyllosilicate mineralogical composition (paragonite-pyrophyllite exchange) and K–Ar signatures (Akker et al., 2021). It has already been suggested that re- and neocrystallization are efficient temperature-controlled mechanisms for the precipitation of fine-grained phyllosilicates (e.g., Airaghi et al., 2017; Akker et al., 2021; Berger et al., 2017). Considering foliation evolution and growth, we therefore conclude that the aligned growth of syntectonic authigenic phyllosilicates due to pressure-dissolution-precipitation creep becomes the dominant foliation-forming mechanism at T > 230 C, going hand in hand with near-complete replacement and recycling of detrital phyllosilicates (Akker et al., 2021).

5.3. Implications for the wedge-scale

5.3.1. Finite strain, mechanical anisotropy, and strength

Our microstructural observations indicate that penetrative, interconnected, secondary foliations form by pressure-dissolution-precipitation creep in samples that reached temperatures >230 °C, regardless of the bulk mineralogy. Below this threshold temperature, foliations are primary (bedding). Up to T = 330 °C, foliation spacing decreases from ~60 μm to about 20 μm. Our microchemical data show that the interconnected foliation domains mainly consist of neo- and recrystallized phyllosilicates. Thus, the decrease in foliation spacing indicates an increase in the volume proportion of recrystallized and newly formed micas (Fig. 13). Similarly, larger aspect ratios of clasts in more tightly spaced microlithons imply a larger volume proportion of recrystallized or newly precipitated calcite or phyllosilicates. Since pressure-dissolution-precipitation creep is by far the most important deformation mechanism and responsible for the generation of all secondary minerals, it is reasonable to assume that a systematic increase in foliation density and volume proportion indicates larger finite strains, as demonstrated for solution-foliation spacing in micritic limestones (Alvarez et al., 1978). The documented deformation reflects non-coaxial deformation conditions, as demonstrated by regional asymmetric, vergent folding, asymmetric clasts (Fig. 9a and b), and micro-scale S–C fabrics (Figs. 10a and 11c). Progressive large non-coaxial deformation induces a continuous strain-dependent parallelization of the spaced foliation defined by aligned phyllosilicates, which results in a strongly anisotropic, layered fabric that introduces mechanical and transport anisotropy into the rock package. The mechanical anisotropy is immediately evident in outcrop: because of their easy cleavability along the foliation planes, the slates of the Northhelvetic Flysch have been mined for decades as roofing tiles and blackboards (Donath, 1964; Gasser and Den Brok, 2008; McLamore and Gray, 1967). Moreover, deformation experiments on shales and slates clearly demonstrate anisotropy of elastic properties (wave velocities, elastic moduli) and strength (Chen et al., 2016; Debecker and Vervoort, 2009; Donath, 1961; McLamore and Gray, 1967). Since the main deformation mechanism responsible for foliation development is pressure-dissolution-precipitation creep, a process characterised by fluid-assisted chemical mass transfer, it is obvious that material fluxes, and hence synkinematic transport properties, were directional and controlled by the far-field tectonic stress (e.

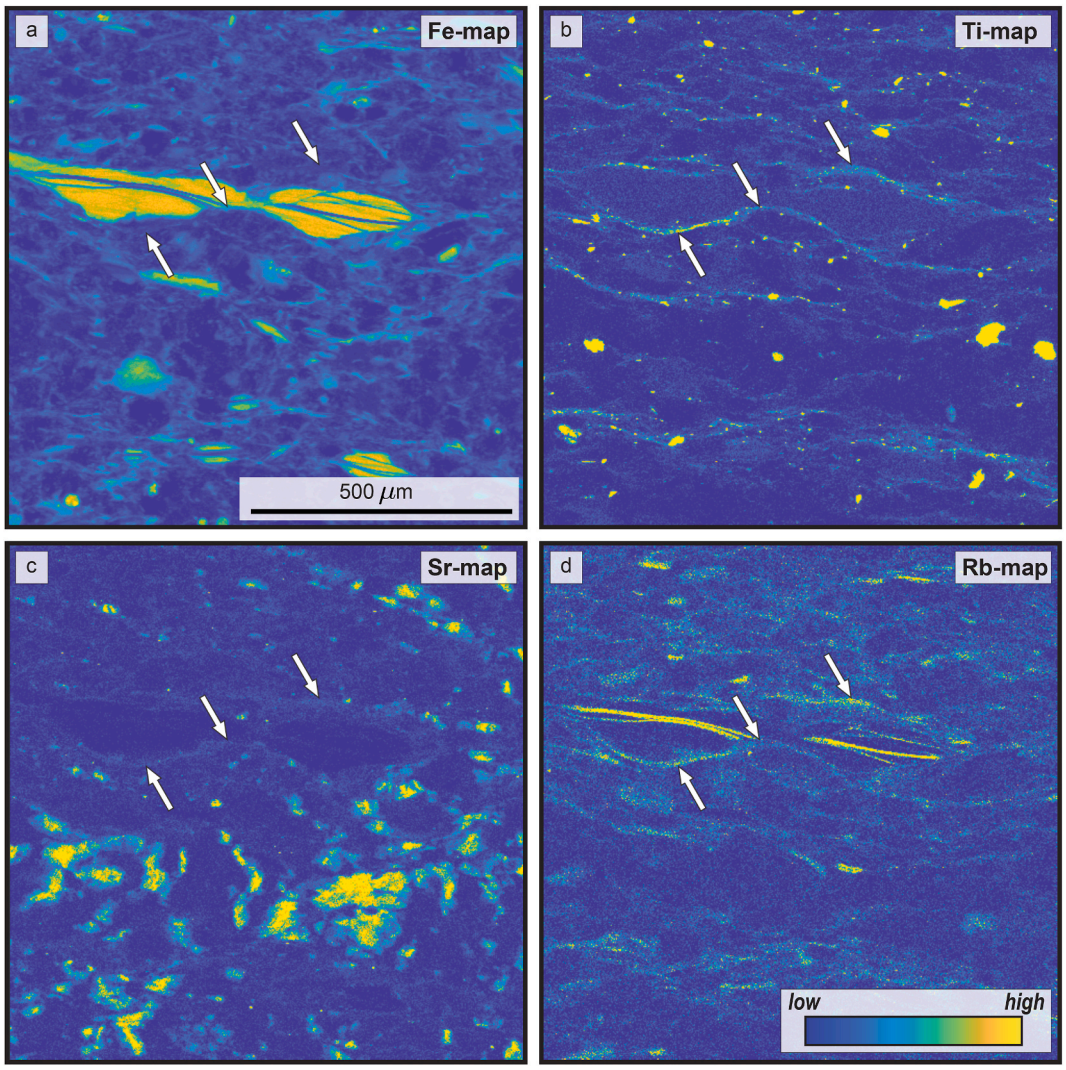

Fig. 12. Four element maps from SXFM show one large detrital phyllosilicate grain (white mica-chlorite mixed aggregate) in a finer-grained matrix with foliation planes. The foliation planes show a homogeneously distributed Ti and Rb concentration. White mica interlayers in the mixed aggregates are relatively enriched in Rb.

g., Figs. 10b and 12). Our observations thus support the notion that phyllosilicate-rich secondary foliations formed by pressure-dissolution-precipitation creep constitute the main fluid pathways for the slow aseismic ductile deformation of rocks in the inner wedge (Bell and Cuff, 1989; Etheridge et al., 1984; Marshak and Engelder, 1985). Below T ≈ 230 °C, the main transport mechanism for distributed slow fluid flow is Darcy flow through the primary pore space of the sedimentary rocks (e.g., Dielforder et., 2016a; Dielforder et al., 2015).

Generally, rock strength in an accretionary wedge increases from the outer to the inner wedge, i.e., from unconsolidated sediment to consolidated sedimentary rock, the latter gaining further strength with increasing metamorphic grade (e.g., Dielforder et., 2016a; Dielforder et al., 2015; Lockner and Byerlee, 1986; Moore and Saffer, 2001). The main microphysical reasons for this strength increase are mechanical and chemical pore closure and recrystallization of grains, leading to the formation of cohesive rocks with low porosity and fairly equant, interlocking grains. However, this general strength gain may, at least partially, be compensated by the observed formation of deformation-induced secondary foliations forming interconnected weak layers (Montési, 2013). It is generally accepted that the interconnectivity of weak minerals defines the strength of polymineralic rocks (e.g., Handy et al., 1999; Handy, 1990, 1994). Experimental work suggests that phyllosilicate seams respond to non-coaxial shearing by frictional-viscous flow, i.e., frictional sliding along established phyllosilicate layers promoted by fluid-assisted pressure solution (Bos and Spiers, 2002; Fagereng and Den Hartog, 2017; French and Condit, 2019; Handy et al., 1999; Rutter, 1983). Hence, we suspect that the observed secondary phyllosilicate-rich foliations endow the inner wedge with a bulk rheology consistent with frictional-viscous flow, strongly mediated by pressure dissolution (Niemeijer and Spiers, 2005).

5.3.2. *Continuous versus episodic fluid fluxes*

Despite aforementioned permeability anisotropies and localized micro-scale fluid fluxes, it remains unsolved whether foliations and resulting patterns in composition are indicative of open-system processes, including advection and fluid flow over large distances, or closed-system processes characterized by local diffusion over short transport distances (Bell and Cuff, 1989; Lentz, 1999; Vernon, 1998).

Our observations demonstrate that the high-grade foliations mainly consist of neo- and re-crystallised phyllosilicates formed by pressure-dissolution-precipitation creep, a process requiring fluids. Re-and neocrystallization of hydrous phyllosilicates points to a local fluid source component. However, based on the available data, we cannot determine if this fluid was brought in from far away (open-system scenario) or largely sourced locally from pre-existing pore fluids and in-situ dehydration reactions (closed-system).

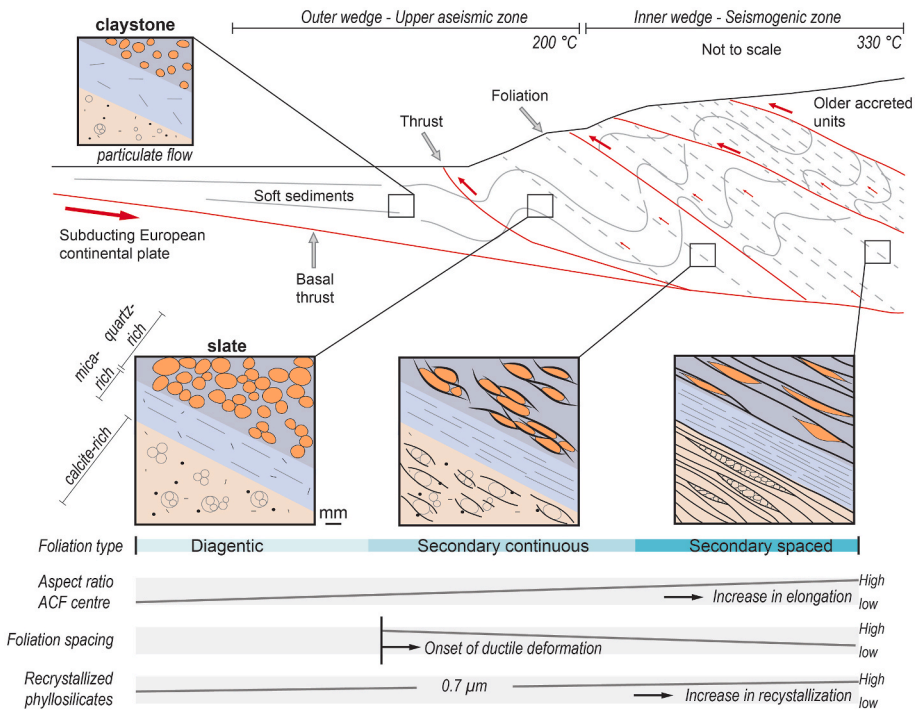

Fig. 13. Evolving microstructures with progressive accretion, sketch of accretionary wedge modified after Dielforder et al. (2016a). In the outer wedge sedimentary sequences of alternating layers of carbonate, clay, and sandstone deform dominantly by particulate flow. With increasing metamorphic gradient and related background strain, a diagenetic micro-fabric develops, followed by a secondary continuous foliation, and finally by a narrow spaced foliation. The aspect ratio of the ACF centre increases, and the foliation spacing decreases with increasing metamorphic temperature due to increasing pressure-dissolution-precipitation creep. The formation of a secondary foliation marks the onset of ductile deformation by dissolution-precipitation creep. Dissolution-precipitation is supported by an increase in recrystallization of phyllosilicates with increasing metamorphic grade (Akker et al., 2021). The boundary between outer and inner wedge is as defined by Dielforder et al. (2016a).

Depending on the ratio between fluid liberation and foliation-parallel fluid escape, pore fluid pressures can build up. Given the deep paleo-depths required to reach the 200–350 °C temperature range, pore fluid pressures close to lithostatic pressures have to be expected (high pore fluid pressure ratio), keeping the effective stresses low in the accretionary wedge (e.g. Dielforder (2017); Etheridge et al. (1984); Moore and Vrolijk (1992); Von Hagke et al. (2014); Wang and Hu (2006). Hence, small variations in tectonics stresses may induce hydrofracturing (e.g. Donath (1961); Shea Jr and Kronenberg (1993). Within the inner wedge, we observe foliation-parallel calcite and quartz veins (see also Dielforder et al. (2015); Dielforder et al. (2016a). These structures reflect the hydraulic fracturing of the weak foliation planes and suggest at least temporarily enhanced fracture-permeabilities and fluid fluxes (Fig. 2a).

We therefore expect a continuous but slow background fluid flux assisting pressure-dissolution-precipitation creep, which is temporarily locally enhanced by episodic hydrofracturing events, before becoming reduced again by vein precipitation (Fisher, 1996; Meneghini et al., 2009; Raimbourg et al., 2015; Roo, 1989). Since Dielforder et al. (2015) suggest that megathrust earthquakes along basal thrusts can be considered as source for co-seismic veining within the studied Flysch units, we may speculate that high-speed fracture-induced fluid fluxes occurred episodically. However, more work is necessary to assess the dimensions, rates, and fluid volumes at different scales in the wedge to test this notion.

6. Conclusion

Typical slate microfabrics are defined by phyllosilicate-rich foliation planes and clasts (mostly quartz and calcite), the latter sometimes forming microlithons. All investigated slates show a large compositional heterogeneity due to original sedimentary layering. Such initial sedimentary-compositional variations, as well as differences in grain packing and density, distribution of phases, and grain sizes, result in contrasting microfabrics for different microlayers in the slates.

Despite such original compositional variation of sediments in underfilled foreland basins, slate microfabrics evolve from a diagenetic foliation in the outer wedge to a secondary continuous and narrow spaced foliation towards the deepest parts of the inner wedge and evolve as function of progressive accretion and increasing metamorphic grade. These evolving foliations are defined by accumulation and progressive interconnection of phyllosilicate seams, in which individual phyllosilicate grains show a strong SPO. Detrital quartz and calcite (including fossils) clasts become affected by anisotropic pressure-dissolution-precipitation creep, also resulting in elongated grains with strong SPO. However, such clast and matrix grains become depleted with time and strain along the phyllosilicate seams by progressive dissolution and mass transfer. The processes responsible for foliation formation under non-coaxial deformation conditions comprise mechanical grain rotations in combination with clast/microlithon fracturing and fluid-assisted pressure-dissolution-precipitation creep. Increasing (i) clast/microlithon elongation, (ii) degree of phyllosilicate recrystallization and (iii) interconnection, as well as (iv) decreasing foliation spacing with increasing metamorphic grade indicate that pressure-dissolution-precipitation creep is the dominant deformation mechanism at $T > 230$ °C.

By forming such densely spaced foliations, the microstructure accommodates strain expressed on the wedge-scale. We therefore conclude that the evolving microstructure may not only be a result of metamorphic grade but also of increasing background strain in the wedge. The resulting microstructural anisotropies and their changes in space and time have important implications for the physico-chemical properties of accretionary wedges such as fluid liberations and fluxes, rock mechanics, as well as seismicity.

Author contributions

MH and AB designed the project. Together with IVA, MH and AB collected the samples and IVA carried out the XRD analysis and microstructural characterisation including SEM work. JK together with IVA performed the BIB-SEM analysis. IVA together with CES, MWMJ and CMK carried out the SXFM measurements. Image analysis was carried out by CES and IVA. IVA analysed all data and prepared the manuscript with contributions from all authors.

Declaration of competing interest

The authors declare that they have no known competing financial interests or personal relationships that could have appeared to influence the work reported in this paper.

Acknowledgements

For this project, funding has been received from the Swiss National Science Foundation (SNSF; grant number 162340). Synchrotron X-ray fluorescence microscopy (SXFM) was undertaken on the X-ray Fluorescence Microscopy (XFM) beamline at the Australian Synchrotron, part of ANSTO. We thank two anonymous reviewers for their constructive and detailed reviews.

References

Airaghi, L., Lanari, P., de Sigoyer, J., Guillot, S., 2017. Microstructural vs compositional preservation and pseudomorphic replacement of muscovite in deformed metapelites from the Longmen Shan (Sichuan, China). Lithos 282, 262–280.
Akker, I.V., 2020. The Evolution of Slate Microstructures during the Accretion of Foreland Basin Sediments and Implications for Mechanical Strength, Fluid Flow and Seismicity in Accretionary Wedges (Unpublished). Dissertation, Institute of Geological Sciences, Faculty of Science).
Akker, I.V., Berger, A., Zwingmann, H., Todd, A., Schrank, C.E., Jones, M.W., Kewish, C. M., Schmid, T.C., Herwegh, M., 2021. Structural and chemical resetting processes in white mica and their effect on K-Ar data during low temperature metamorphism. Tectonophysics 800.
Alvarez, W., Engelder, T., Geiser, P.A., 1978. Classification of solution cleavage in pelagic limestones. Geology 6, 263–266.
Bell, T., Cuff, C., 1989. Dissolution, solution transfer, diffusion versus fluid flow and volume loss during deformation/metamorphism. J. Metamorph. Geol. 7, 425–447.
Berger, A., Engi, M., Erne-Schmid, S., Glotzbach, C., Spiegel, C., de Goede, R., Herwegh, M., 2020. The relation between peak metamorphic temperatures and subsequent cooling during continent–continent collision (western Central Alps, Switzerland). Swiss J. Geosci. 113, 1–18.
Berger, A., Herwegh, M., Schwarz, J.-O., Putlitz, B., 2011. Quantitative analysis of crystal/grain sizes and their distributions in 2D and 3D. J. Struct. Geol. 33, 1751–1763.
Berger, A., Wehrens, P., Lanari, P., Zwingmann, H., Herwegh, M., 2017. Microstructures, mineral chemistry and geochronology of white micas along a retrograde evolution: an example from the Aar massif (Central Alps, Switzerland). Tectonophysics 721, 179–195.
Bons, A., Drury, M., Schryvers, D., Zwart, H., 1990. The nature of grain boundaries in slates implications for mass transport processes during low temperature metamorphism. Phys. Chem. Miner. 17, 402–408.
Bons, A.J., 1988. Intracrystalline deformation and slaty cleavage development in very low-grade slates from the Central Pyrenees. PhD thesis. In: Zwart, H.J., Drury, Martyn (Eds.), Faculteit Aardwetenschappen. Utrecht University, Netherlands. Repository (Dissertation).
Borradaile, G.J., 1981. Particulate flow of rock and the formation of cleavage. Tectonophysics 72, 305–321.
Bos, B., Peach, C., Spiers, C., 2000. Frictional-viscous flow of simulated fault gouge caused by the combined effects of phyllosilicates and pressure solution. Tectonophysics 327, 173–194.
Bos, B., Spiers, C., 2001. Experimental investigation into the microstructural and mechanical evolution of phyllosilicate-bearing fault rock under conditions favouring pressure solution. J. Struct. Geol. 23, 1187–1202.
Bos, B., Spiers, C.J., 2002. Frictional-viscous flow of phyllosilicate-bearing fault rock: microphysical model and implications for crustal strength profiles. J. Geophys. Res.: Solid Earth 107. ECV 1-1-ECV 1-13.
Bouchez, J.-L., 1977. Plastic deformation of quartzites at low temperature in an area of natural strain gradient. Tectonophysics 39, 25–50.
Chen, Y.-F., Wei, K., Liu, W., Hu, S.-H., Hu, R., Zhou, C.-B., 2016. Experimental characterization and micromechanical modelling of anisotropic slates. Rock Mech. Rock Eng. 49, 3541–3557.
Cosgrove, J., 1976. The formation of crenulation cleavage. J. Geol. Soc. 132, 155–178.
de Meer, S., Spiers, C.J., Peach, C.J., Watanabe, T., 2002. Diffusive properties of fluid-filled grain boundaries measured electrically during active pressure solution. Earth Planet Sci. Lett. 200, 147–157.
Debecker, B., Vervoort, A., 2009. Experimental observation of fracture patterns in layered slate. Int. J. Fract. 159, 51–62.
Den Hartog, S.A., Spiers, C.J., 2014. A microphysical model for fault gouge friction applied to subduction megathrusts. J. Geophys. Res.: Solid Earth 119, 1510–1529.
Dielforder, A., 2017. Constraining the strength of megathrusts from fault geometries and application to the Alpine collision zone. Earth Planet Sci. Lett. 474, 49–58.
Dielforder, A., Berger, A., Herwegh, M., 2016a. The accretion of foreland basin sediments during early stages of continental collision in the European Alps and similarities to accretionary wedge tectonics. Tectonics 35, 2216–2238.
Dielforder, A., Vollstaedt, H., Vennemann, T., Berger, A., Herwegh, M., 2015. Linking megathrust earthquakes to brittle deformation in a fossil accretionary complex. Nat. Commun. 6.
Dielforder, A.R., Herwegh, M., Berger, A., 2016b. The Accretion of Underfilled Foreland Basin Sediments and its Implication for the Prograde Evolution of Collisional Orogens: an Integrative Structural, Mechanical and Geochemical Perspective. Institut für Geologie.
Ditullio, L., Byrne, T., 1990. Deformation paths in the shallow levels of an accretionary prism: the Eocene Shimanto belt of southwest Japan. Geol. Soc. Am. Bull. 102, 1420–1438.
Donath, F., 1964. Strength Variation and Deformational Behavior in Anisotropic Rock. State of Stress in the Earth's Crust 281.
Donath, F.A., 1961. Experimental study of shear failure in anisotropic rocks. Geol. Soc. Am. Bull. 72, 985–989.
Durney, D., 1972a. Solution-transfer, an important geological deformation mechanism. Nature 235, 315–317.
Durney, D., 1976. A Discussion on natural strain and geological structure-Pressure-solution and crystallization deformation. Phil. Trans. Roy. Soc. Lond. Math. Phys. Sci. 283, 229–240.
Durney, D.W., 1972b. Deformation History of the Western Helvetic Nappes, Valais, Switzerland. Imperial College London.
Ebert, A., Herwegh, M., Pfiffner, A., 2007. Cooling induced strain localization in carbonate mylonites within a large-scale shear zone (Glarus thrust, Switzerland). J. Struct. Geol. 29, 1164–1184.
Elphick, K.E., Sloss, C.R., Regenauer-Lieb, K., Schrank, C.E., 2021. Distribution, microphysical properties, and tectonic controls of deformation bands in the Miocene subduction wedge (Whakataki Formation) of the Hikurangi subduction zone. Solid Earth 12, 141–170.
Engelder, T., Marshak, S., 1985. Disjunctive cleavage formed at shallow depths in sedimentary rocks. J. Struct. Geol. 7, 327–343.
Etheridge, M., Hobbs, B., 1974. Chemical and deformational controls on recrystallization of mica. Contrib. Mineral. Petrol. 43, 111–124.
Etheridge, M., Wall, V., Vernon, R., 1983. The role of the fluid phase during regional metamorphism and deformation. J. Metamorph. Geol. 1, 205–226.
Etheridge, M.A., Wall, V., Cox, S., Vernon, R., 1984. High fluid pressures during regional metamorphism and deformation: implications for mass transport and deformation mechanisms. J. Geophys. Res.: Solid Earth 89, 4344–4358.
Fagereng, Å., Den Hartog, S.A., 2017. Subduction megathrust creep governed by pressure solution and frictional–viscous flow. Nat. Geosci. 10, 51–57.
Fagereng, Å., Remitti, F., Sibson, R.H., 2011. Incrementally developed slickenfibers—geological record of repeating low stress-drop seismic events? Tectonophysics 510, 381–386.
Fagereng, Å., Savage, H., Morgan, J., Wang, M., Meneghini, F., Barnes, P., Bell, R., Kitajima, H., McNamara, D., Saffer, D., 2019. Mixed deformation styles observed on a shallow subduction thrust, Hikurangi margin, New Zealand. Geology 47, 872–876.
Fisher, D.M., 1996. Fabrics and Veins in the Forearc: A Record of Cyclic Fluid Row at Depths Of< 15 Km, Subduction Top to Bottom, 1996. Blackwell Publishing Ltd, pp. 75–89.
French, M.E., Condit, C.B., 2019. Slip partitioning along an idealized subduction plate boundary at deep slow slip conditions. Earth Planet Sci. Lett. 528, 115828.
Frey, M., Hunziker, J., Frank, W., Bocquet, J., Dal Piaz, G., Jäger, E., Niggli, E., 1974. Alpine metamorphism of the Alps: a review. Schweiz. Mineral. Petrogr. Mitt 54, 247–290.
Frey, M., Teichmüller, M., Teichmüller, R., Mullis, J., Künzi, B., Breitschmid, A., Gruner, U., Schwizer, B., 1980. Very low-grade metamorphism in external parts of the Central Alps: illite crystallinity, coal rank and fluid inclusion data. Eclogae Geol. Helv. 73, 173–203.
Gasser, D., Den Brok, B., 2008. Tectonic evolution of the Engi slates, Glarus alps, Switzerland. Swiss J. Geosci. 101, 311–322.
Gratier, J.-P., Dysthe, D.K., Renard, F., 2013a. The role of pressure solution creep in the ductility of the Earth's upper crust. Advances in Geophysics. Elsevier 47–179.
Gratier, J.-P., Thouvenot, F., Jenatton, L., Tourette, A., Doan, M.-L., Renard, F., 2013b. Geological control of the partitioning between seismic and aseismic sliding behaviours in active faults: evidence from the Western Alps. France. Tectonophysics 600, 226–242.
Gratier, J., 1987. Pressure solution-deposition creep and associated tectonic differentiation in sedimentary rocks. Geological Society, London, Special Publications 29, 25–38.
Gray, D., 1978. Cleavages in deformed psammitic rocks from southeastern Australia: their nature and origin. Geol. Soc. Am. Bull. 89, 577–590.
Groshong Jr., R.H., 1988. Low-temperature deformation mechanisms and their interpretation. Geol. Soc. Am. Bull. 100, 1329–1360.
Handy, M., Wissing, S., Streit, L., 1999. Frictional–viscous flow in mylonite with varied bimineralic composition and its effect on lithospheric strength. Tectonophysics 303, 175–191.
Handy, M.R., 1990. The solid-state flow of polymineralic rocks. J. Geophys. Res.: Solid Earth 95, 8647–8661.
Handy, M.R., 1994. Flow laws for rocks containing two non-linear viscous phases: a phenomenological approach. J. Struct. Geol. 16, 287–301.
Heald, M.T., 1955. Stylolites in sandstones. J. Geol. 63, 101–114.
Heilbronner, R.P., 1992. The autocorrelation function: an image processing tool for fabric analysis. Tectonophysics 212, 351–370.
Herwegh, M., Hürzeler, J.-P., Pfiffner, O.A., Schmid, S.M., Abart, R., Ebert, A., 2008. The Glarus thrust: excursion guide and report of a field trip of the swiss tectonic studies Group (swiss Geological society, 14.–16. 09. 2006). Swiss J. Geosci. 101, 323–340.

Herwegh, M., Jenni, A., 2001. Granular flow in polymineralic rocks bearing sheet silicates: new evidence from natural examples. Tectonophysics 332, 309–320.
Ho, N.-C., Peacor, D.R., Van Der Pluijm, B.A., 1996. Contrasting roles of detrital and authigenic phyllosilicates during slaty cleavage development. J. Struct. Geol. 18, 615–623.
Howard, D.L., de Jonge, M.D., Afshar, N., Ryan, C.G., Kirkham, R., Reinhardt, J., Kewish, C.M., McKinlay, J., Walsh, A., Divitcos, J., 2020. The XFM beamline at the Australian Synchrotron. J. Synchrotron Radiat. 27, 1447–1458.
Hunziker, J., Frey, M., Clauer, N., Dallmeyer, R., Friedrichsen, H., Flehmig, W., Hochstrasser, K., Roggwiler, P.t., Schwander, H., 1986. The evolution of illite to muscovite: mineralogical and isotopic data from the Glarus Alps, Switzerland. Contrib. Mineral. Petrol. 92, 157–180.
Hyndman, R., Wang, K., Yuan, T., Spence, G., 1993. Tectonic sediment thickening, fluid expulsion, and the thermal regime of subduction zone accretionary prisms: the Cascadia margin off Vancouver Island. J. Geophys. Res.: Solid Earth 98, 21865–21876.
Ishii, K., 1988. Grain growth and re-orientation of phyllosilicate minerals during the development of slaty cleavage in the South Kitakami Mountains, northeast Japan. J. Struct. Geol. 10, 145–154.
Jeffery, G.B., 1922. The motion of ellipsoidal particles immersed in a viscous fluid. Proc. R. Soc. Lond. - Ser. A Contain. Pap. a Math. Phys. Character 102, 161–179.
Kawabata, K., Tanaka, H., Kimura, G., 2007. Mass transfer and pressure solution in deformed shale of accretionary complex: examples from the Shimanto Belt, southwestern Japan. J. Struct. Geol. 29, 697–711.
Kimura, G., Kitamura, Y., Hashimoto, Y., Yamaguchi, A., Shibata, T., Ujiie, K., Okamoto, S.y., 2007. Transition of accretionary wedge structures around the up-dip limit of the seismogenic subduction zone. Earth Planet Sci. Lett. 255, 471–484.
Klaver, J., Desbois, G., Urai, J.L., Littke, R., 2012. BIB-SEM study of the pore space morphology in early mature Posidonia Shale from the Hils area, Germany. Int. J. Coal Geol. 103, 12–25.
Knipe, R., 1981. The interaction of deformation and metamorphism in slates. Tectonophysics 78, 249–272.
Lahfid, A., Beyssac, O., Deville, E., Negro, F., Chopin, C., Goffé, B., 2010. Evolution of the Raman spectrum of carbonaceous material in low-grade metasediments of the Glarus Alps (Switzerland). Terra. Nova 22, 354–360.
Lentz, D., 1999. Deformation-induced mass transfer in felsic volcanic rocks hosting the Brunswick No. 6 massive-sulfide deposit, New Brunswick; geochemical effects and petrogenetic implications. Can. Mineral. 37, 489–512.
Lihou, J.C., Allen, P.A., 1996. Importance of inherited rift margin structures in the early North Alpine Foreland Basin, Switzerland. Basin Res. 8, 425–442.
Lockner, D., Byerlee, J., 1986. Laboratory measurements of velocity-dependent frictional strength. In: Open-File Report. U.S. Geological Survey. https://doi.org/10.3133/ofr86417. USGS Numbered Series, Series number: 86-417.
Maltman, A., 2012. The Geological Deformation of Sediments. Springer Science & Business Media.
March, A., 1932. Mathematische Theorie der Regelung nach der Korngestah bei affiner Deformation. Z. für Kristallogr. - Cryst. Mater. 81, 285–297.
Marlow, P., Etheridge, M., 1977. Development of a layered crenulation cleavage in mica schists of the Kanmantoo Group near Macclesfield, South Australia. Geol. Soc. Am. Bull. 88, 873–882.
Marshak, S., Engelder, T., 1985. Development of cleavage in limestones of a fold-thrust belt in eastern New York. J. Struct. Geol. 7, 345–359.
McLamore, R., Gray, K., 1967. The Mechanical Behavior of Anisotropic Sedimentary Rocks.
Meneghini, F., Marroni, M., Moore, J., Pandolfi, L., Rowe, C., 2009. The processes of underthrusting and underplating in the geologic record: structural diversity between the Franciscan Complex (California), the Kodiak Complex (Alaska) and the Internal Ligurian Units (Italy). Geol. J. 44, 126–152.
Milnes, A.G., Pfiffner, O.-A., 1977. Structural development of the Infrahelvetic complex, eastern Switzerland. Eclogae Geol. Helv. 70, 83–95.
Montési, L.G., 2013. Fabric development as the key for forming ductile shear zones and enabling plate tectonics. J. Struct. Geol. 50, 254–266.
Moore, G.F., Shipley, T., Stoffa, P., Karig, D., Taira, A., Kuramoto, S., Tokuyama, H., Suyehiro, K., 1990. Structure of the Nankai Trough accretionary zone from multichannel seismic reflection data. J. Geophys. Res.: Solid Earth 95, 8753–8765.
Moore, J.C., Saffer, D., 2001. Updip limit of the seismogenic zone beneath the accretionary prism of southwest Japan: an effect of diagenetic to low-grade metamorphic processes and increasing effective stress. Geology 29, 183–186.
Moore, J.C., Vrolijk, P., 1992. Fluids in accretionary prisms. Rev. Geophys. 30, 113–135.
Morgan, J., Karig, D., 1995. Kinematics and a balanced and restored cross-section across the toe of the eastern Nankai accretionary prism. J. Struct. Geol. 17, 31–45.
Nenna, F., Aydin, A., 2011. The formation and growth of pressure solution seams in clastic rocks: a field and analytical study. J. Struct. Geol. 33, 633–643.
Nibourel, L., Berger, A., Egli, D., Luensdorf, N.K., Herwegh, M., 2018. Large vertical displacements of a crystalline massif recorded by Raman thermometry. Geology 46, 879–882.
Niemeijer, A., Spiers, C., 2005. Influence of phyllosilicates on fault strength in the brittle-ductile transition: insights from rock analogue experiments. Geological Society, London, Special Publications 245, 303–327.
Norris, R., Bishop, D., 1990. Deformed conglomerates and textural zones in the Otago schists, South Island, New Zealand. Tectonophysics 174, 331–349.
Oertel, G., 1983. The relationship of strain and preferred orientation of phyllosilicate grains in rocks—a review. Tectonophysics 100, 413–447.
Oleskevich, D., Hyndman, R., Wang, K., 1999. The updip and downdip limits to great subduction earthquakes: thermal and structural models of Cascadia, south Alaska, SW Japan, and Chile. J. Geophys. Res.: Solid Earth 104, 14965–14991.
Orange, D.L., Geddes, D.S., Moore, J.C., 1993. Structural and Fluid Evolution of a Young Accretionary Complex: the Hoh Rock Assemblage of the Western Olympic Peninsula, 105. Geological Society of America Bulletin, Washington, pp. 1053–1075.
Palazzin, G., Raimbourg, H., Famin, V., Jolivet, L., Kusaba, Y., Yamaguchi, A., 2016. Deformation processes at the down-dip limit of the seismogenic zone: the example of Shimanto accretionary complex. Tectonophysics 687, 28–43.
Passchier, C.W., Trouw, R.A., 2005. Microtectonics. Springer Science & Business Media.
Pfiffner, O.A., Ramsay, J., Schmid, S., 2011. Structural map of the helvetic zone of the Swiss alps. Geological special map 1.
Plessman, W.v., 1964. Gesteinslosung, ein Hauptfaktor beim Schieferungsprozess. Geol. Mitt. 4, 69 8.
Rahl, J.M., Brandon, M.T., Deckert, H., Ring, U., Mortimer, N., 2011. Tectonic significance of ductile deformation in low-grade sandstones in the Mesozoic Otago subduction wedge, New Zealand. Am. J. Sci. 311, 27–62.
Rahn, M., Mullis, J., Erdelbrock, K., Frey, M., 1995. Alpine metamorphism in the north Helvetic flysch of the Glarus-Alps, Switzerland. Eclogae Geol. Helv. 88, 157–178.
Railsback, L.B., 1993. Lithologic controls on morphology of pressure-dissolution surfaces (stylolites and dissolution seams) in Paleozoic carbonate rocks from the mideastern United States. J. Sediment. Res. 63, 513–522.
Raimbourg, H., Tadahiro, S., Asuka, Y., Haruka, Y., Kimura, G., 2009. Horizontal shortening versus vertical loading in accretionary prisms. G-cubed 10.
Raimbourg, H., Vacelet, M., Ramboz, C., Famin, V., Augier, R., Palazzin, G., Yamaguchi, A., Kimura, G., 2015. Fluid circulation in the depths of accretionary prisms: an example of the Shimanto Belt. Kyushu, Japan. Tectonophysics 655, 161–176.
Roo, J.D., 1989. Mass transfer and preferred orientation development during extensional microcracking in slate-belt folds, Elura Mine, Australia. J. Metamorph. Geol. 7, 311–322.
Rueden, C.T., Schindelin, J., Hiner, M.C., DeZonia, B.E., Walter, A.E., Arena, E.T., Eliceiri, K.W., 2017. ImageJ2: ImageJ for the next generation of scientific image data. BMC Bioinf. 18, 529.
Rutter, E., 1976. A discussion on natural strain and geological structure-the kinetics of rock deformation by pressure solution. Phil. Trans. Roy. Soc. Lond. Math. Phys. Sci. 283, 203–219.
Rutter, E., 1983. Pressure solution in nature, theory and experiment. J. Geol. Soc. 140, 725–740.
Ryan, C.G., Etschmann, B.E., Vogt, S., Maser, J., Harland, C.L., van Achterbergh, E., Legnini, D., 2005. Nuclear microprobe - synchrotron synergy: towards integrated quantitative real-time elemental imaging using PIXE and SXRF. Nucl. Instrum. Methods Phys. Res. B 231, 183–188.
Ryan, C.G., Jamieson, D.N., 1993. Dynamic analysis: on-line quantitative PIXE microanalysis and its use in overlap-resolved elemental mapping. Nucl. Instrum. Methods Phys. Res. B 77, 203–214.
Saffer, D.M., Tobin, H.J., 2011. Hydrogeology and mechanics of subduction zone forearcs: fluid flow and pore pressure. Annu. Rev. Earth Planet Sci. 39, 157–186.
Sample, J.C., Moore, J.C., 1987. Structural style and kinematics of an underplated slate belt, Kodiak and adjacent islands, Alaska. Geol. Soc. Am. Bull. 99, 7–20.
Schmid, S.M., 1975. The Glarus Overthrust: Field Evidence and Mechanical Model.
Schrank, C.E., Karrech, A., Boutelier, D.A., Regenauer-Lieb, K., 2015. Ductile deformation of single inclusions in simple shear with a finite-strain hyperelastoviscoplastic rheology. Ductile Shear Zones: From Micro-to Macro-scales 46–58.
Shea Jr., W.T., Kronenberg, A.K., 1993. Strength and anisotropy of foliated rocks with varied mica contents. J. Struct. Geol. 15, 1097–1121.
Shea, W.T., Kronenberg, A.K., 1992. Rheology and deformation mechanisms of an isotropic mica schist. J. Geophys. Res.: Solid Earth 97, 15201–15237.
Shinn, E.A., Robbin, D.M., 1983. Mechanical and chemical compaction in fine-grained shallow-water limestones. J. Sediment. Res. 53, 595–618.
Sorby, H., 1853. On the origin of slaty cleavage. Edinburgh New Philosophical Journal 55.
Turnbull, I., Mortimer, N., Craw, D., 2001. Textural zones in the haast schist—a reappraisal. N. Z. J. Geol. Geophys. 44, 171–183.
Ujiie, K., Kimura, G., 2014. Earthquake faulting in subduction zones: insights from fault rocks in accretionary prisms. Progress in Earth and Planetary Science 1, 7.
van den Ende, M.P., Niemeijer, A., Spiers, C., 2019. Influence of grain boundary structural evolution on pressure solution creep rates. J. Geophys. Res.: Solid Earth 124, 10210–10230.
van der Pluijm, B.A., Ho, N.-C., Peacor, D.R., Merriman, R.J., 1998. Contradictions of slate formation resolved? Nature 392, 348.
Vannucchi, P., Bettelli, G., 2002. Mechanisms of subduction accretion as implied from the broken formations in the Apennines, Italy. Geology 30, 835–838.
Vernon, R., 1998. Chemical and volume changes during deformation and prograde metamorphism of sediments. Geological Society, London, Special Publications 138, 215–246.

Von Hagke, C., Oncken, O., Evseev, S., 2014. Critical taper analysis reveals lithological control of variations in detachment strength: an analysis of the Alpine basal detachment (Swiss Alps). G-cubed 15, 176–191.
Waldron, H.M., Sandiford, M., 1988. Deformation volume and cleavage development in metasedimentary rocks from the Ballarat slate belt. J. Struct. Geol. 10, 53–62.
Wang, K., Hu, Y., 2006. Accretionary prisms in subduction earthquake cycles: the theory of dynamic Coulomb wedge. J. Geophys. Res.: Solid Earth 111.
Wenk, H.-R., Kanitpanyacharoen, W., Ren, Y., 2019. Slate–A new record for crystal preferred orientation. J. Struct. Geol. 125, 319–324.
Weyl, P.K., 1959. Pressure solution and the force of crystallization: a phenomenological theory. J. Geophys. Res. 64, 2001–2025.
Wheeler, J., 1987. The significance of grain-scale stresses in the kinetics of metamorphism. Contrib. Mineral. Petrol. 97, 397–404.
White, S., Knipe, R., 1978. Microstructure and cleavage development in selected slates. Contrib. Mineral. Petrol. 66, 165–174.
Wright, T.O., Platt, L.B., 1982. Pressure dissolution and cleavage in the martinsburg shale. Am. J. Sci. 282, 122–135.